Dense-vapor effects in compressible internal flows

Tosto, Francesco; Lettieri, Claudio; Pini, Matteo; Colonna, Piero

DOI
10.1063/5.0058075

Publication date
2021

Document Version
Final published version

Published in
Physics of Fluids

Dense-vapor effects in compressible internal flows

Cite as: Phys. Fluids **33**, 086110 (2021); https://doi.org/10.1063/5.0058075
Submitted: 26 May 2021 . Accepted: 28 July 2021 . Published Online: 19 August 2021

Francesco Tosto, Claudio Lettieri, Matteo Pini, et al.

Physics of Fluids ARTICLE scitation.org/journal/phf

Dense-vapor effects in compressible internal flows

Cite as: Phys. Fluids **33**, 086110 (2021); doi: 10.1063/5.0058075
Submitted: 26 May 2021 · Accepted: 28 July 2021 ·
Published Online: 19 August 2021

Francesco Tosto, Claudio Lettieri, Matteo Pini,[a] and Piero Colonna

AFFILIATIONS

Propulsion and Power, Delft University of Technology, Kluyverweg 1, 2629 HS Delft, The Netherlands

[a]Author to whom correspondence should be addressed: m.pini@tudelft.nl

ABSTRACT

Paradigmatic compressible one-dimensional flows provide insights regarding the loss mechanisms of fluid machinery components typical of power and propulsion systems, like turbomachines and heat exchangers. Their performance also depends on the working fluid, thus, on both molecular complexity and thermodynamic state. Four typical flow configurations have been investigated, namely, Rayleigh and Fanno flows, mixing of two co-flowing streams, and flow injection into a mainstream. It was found that the Grüneisen parameter allows the quantitative characterization of the influence of molecular complexity on losses. Moreover, the influence of dense vapor effects has been evaluated and assessed in terms of other fluid parameters. The analysis allowed the quantification of how, in Rayleigh flows, the energy transferred as heat is converted into kinetic and internal energy of the fluid, and, in Fanno flows, entropy is generated due to friction. In Rayleigh flow, the fluid at the inlet of the channel must have more energy for the flow to choke, depending on the molecular complexity. Similarly, in Fanno flows and for a given value of the compressibility factor, molecular complexity determines the choking point in the channel, and the higher its value the further downstream is the location. Moreover, for both Fanno and Rayleigh flows, if the flow is subsonic and dense vapor effects are relevant, the Mach number varies non-monotonically along the channel. Finally, it was proven that the amount of entropy generated in mixing flows increases with both the fluid molecular complexity and with the thermodynamic non-ideality of the fluid states.

I. INTRODUCTION

Many chemical and energy conversion processes make use of working fluids which, in certain operating conditions, are in the dense vapor state. Thermodynamic and transport properties, collectively called *thermophysical properties*, of dense vapors differ from those of the so-called ideal gas, see Fig. 1. A fluid is a dense vapor if it is operated in thermodynamic states occurring in proximity of the dew line or near the vapor–liquid critical point. Flows in which the fluid is in these states are affected by large gradients of thermophysical properties.[1] The examples of energy conversion processes in which the working fluid can be affected by the so-called non-ideal compressible fluid dynamic (NICFD) effects are the expansion occurring in the turbine stator of organic Rankine cycle (ORC) power systems,[2,3] the compression occurring in the compressor of supercritical carbon dioxide (sCO_2) power systems,[4] and in the compressor of heat pumps.[5]

Any process affected by non-ideal dense vapor effects makes the design of internal flow components more challenging because standard guidelines for the design of components operated with air or steam as working fluids cannot be employed, as they would lead to incorrect sizing and wrong performance estimations. For example, the design of compressors and turbines generally relies on well-established semiempirical correlations developed for conventional machines using air, combustion gases, or steam as working fluids. These semiempirical models do not provide sufficiently accurate results for turbomachinery operating with dense vapors, see, e.g., Giuffré and Pini.[6] Although methodologies for preliminary fluid dynamic design and optimization of, for example, turbines for ORC power systems,[7–9] compressors for sCO_2 power systems,[10,11] and compressors for heat pumps[12] have been developed, no validated design guidelines for turbomachinery operating partially or completely with the working fluid in the dense vapor thermodynamic region are available yet.

Guidelines specifically developed for the meanline design of these machines would thus provide more accurate predictions of both efficiency and loss breakdown in turbines and compressors operating with dense vapors. Denton[13] first proposed a physics-based loss model for conventional turbomachinery. The model exploits first principles applied to simplified one-dimensional flow configurations to estimate the entropy losses generated by different sources. He identified four loss mechanisms: viscous effects in boundary layers, viscous effects in mixing processes, shock waves, and heat transfer across temperature differences. However, the model is only valid under the ideal gas and

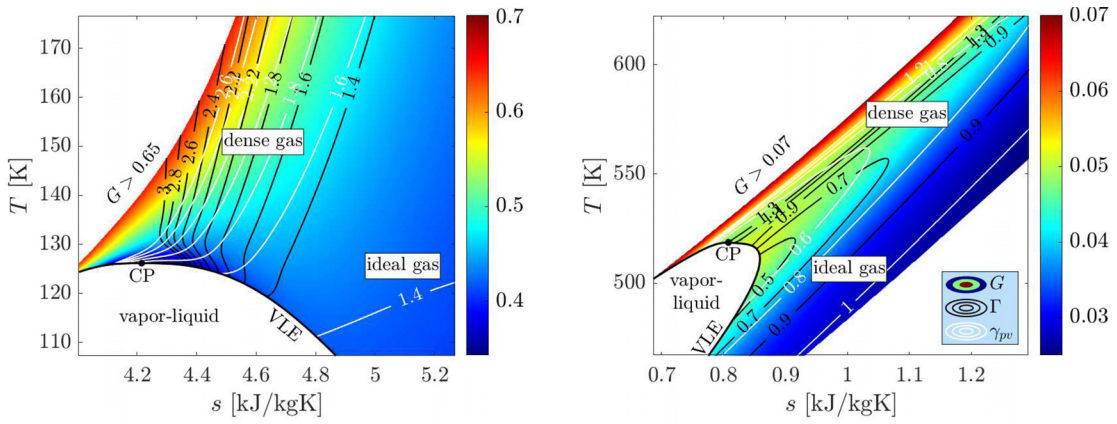

FIG. 1. Temperature-entropy diagram for two fluids with different molecular complexity: (a) CO_2 and (b) hexamethyldisiloxane (siloxane MM). Colored contours report the variation of the Grüneisen parameter. Contours of fundamental derivative Γ (black) and generalized polytropic exponent γ_{pv} (white) are also displayed.

the incompressible flow assumptions. As proven by Giuffré and Pini,[6] the generalization of the model to non-ideal compressible flows allows the development of a design framework which provides more accurate guidelines for unconventional turbomachinery.

Gaining a better physical understanding of how both the working fluid and the non-ideal gas dynamics features affect the flow field is paramount to design efficient fluid machinery components. Following the seminal work of Thompson,[14] the non-ideal fluid dynamics of dense vapor flows is governed by the fundamental derivative of gas dynamics, a fluid thermodynamic property defined as

$$\Gamma \equiv 1 + \frac{\rho}{c}\left(\frac{\partial c}{\partial \rho}\right)_s = \frac{c^4}{2v^3}\left(\frac{\partial^2 v}{\partial p^2}\right)_s, \tag{1}$$

where ρ is the density, c the speed of sound, and s the entropy. The fundamental derivative is related to the variation of the speed of sound with density along isentropic processes: for this reason, the propagation of the waves in dense fluids strongly depends on its value.[15] Equation (1) shows that the sign and the value of Γ can be inferred from the concavity of isentropic lines if displayed on the pressure–volume thermodynamic diagram of the fluid. If $\Gamma > 1$, the sound speed decreases along isentropic compression processes and increases along expansions: this situation is representative of fluid flows occurring during air compression and exhaust gas expansion in turbochargers, or exhaust gas expansion in gas turbines. However, fluid flows for which $\Gamma < 1$ are also possible: in this case, the speed of sound increases over compressions and decreases over expansions. Γ is greater than one if the fluid is in the dilute gas state, that is

$$\Gamma = (\gamma + 1)/2, \tag{2}$$

for the ideal gas, while the line $\Gamma = 1$ delimits vapor states closer to the dew line and to the vapor–liquid critical point of the fluid, for which $Z \equiv pv/(RT) < 1$, where Z is the so-called compressibility factor, see Fig. 1. Furthermore, it is theoretically predicted that so-called Bethe–Zel'dovich–Thompson (BZT) fluids,[14,16,17] whose molecules are rather complex, exhibit a thermodynamic region in the vapor phase where the fundamental derivative is negative. This is a necessary condition for the possibility of attaining non-classical gasdynamic phenomena, such as rarefaction shock waves and compression fans,[18] in flows. The works by Cramer,[19] Zamfirescu,[20] and Kluwick[21] provide an extensive review of the theory of non-classical gas dynamics. The experimental investigations aimed at proving the existence of rarefaction shock waves in BZT fluids were conducted in the past,[22] and are still being performed,[23,24] using siloxanes as working fluids.[17] Moreover, experimental campaigns on dense vapor nozzle flows are currently being conducted with the aim of characterizing non-ideal compressible flows in the presence of shock waves.[25,26] Efforts are also made to enhance the theoretical understanding of compression and expansion phenomena in transonic[27] and supersonic[28–31] dense vapor flows.

Several studies investigating non-ideal compressible effects in characteristic one-dimensional flow processes have already been conducted. Kluwick[32] and Cramer[33] showed that, due to the non-monotonic variation of density with the Mach number, three sonic points rather than a single one may occur during isentropic supersonic expansions of BZT fluids. Therefore, a conventional converging–diverging nozzle is not sufficient to obtain a shock-free expansion from the subsonic to the supersonic regime, but unconventional nozzle shapes consisting of two throats are required. More recently, Guardone and Vimercati[34] outlined a set of exact solutions corresponding to ten different operating regimes in a converging–diverging nozzle using the rather inaccurate van der Waals thermodynamic model for the fluid. Baltadjiev[11] derived approximated relations between stagnation and static variables as a function of the flow Mach number and the isentropic exponents, i.e., $\phi_t/\phi = f(M, \gamma_{pv}, \gamma_{pT})$, where ϕ is a thermodynamic property (enthalpy, pressure, temperature, or density), and the subscript t denotes stagnation quantities. These relations are formally similar to their ideal gas counterparts, the only difference being the use of the generalized isentropic exponents γ_{pv} and γ_{pT} (see Table I) in place of γ. To derive these relations, Baltadjiev[11] assumed the same value of the isentropic exponents for the stagnation and static variables. In addition, they extended the definition of corrected mass flow per unit area $\dot{m}_{corr}$ to the case of isentropic compressible flows of dense vapors. They found that its value depends only on the flow Mach number and the average value of the exponent γ_{pv} over the process. In particular, the

TABLE I. Secondary thermodynamic properties relevant for the study of one-dimensional flows.

Definition	Ideal gas
$\beta_p = \frac{1}{v}\left(\frac{\partial v}{\partial T}\right)_p = \frac{1}{T} + \frac{1}{Z}\left(\frac{\partial Z}{\partial T}\right)_p$	$\frac{1}{T}$
$\beta_T = -\frac{1}{v}\left(\frac{\partial v}{\partial p}\right)_T = \frac{1}{p} + \frac{1}{Z}\left(\frac{\partial Z}{\partial p}\right)_T$	$\frac{1}{p}$
$\gamma_{pv} = \frac{\gamma}{\beta_T p}$	γ
$\gamma_{pT} = \frac{\gamma - 1}{\gamma}\frac{\beta_T p}{\beta_p T}$	$\frac{\gamma-1}{\gamma}$
$\Gamma = 1 + \frac{\rho}{c}\left(\frac{\partial c}{\partial \rho}\right)_s$	$\frac{\gamma+1}{2}$
$G = \frac{1}{\rho c_v}\left(\frac{\partial p}{\partial T}\right)_\rho = \gamma_{pv}\gamma_{Tp}$	$\gamma - 1$
$\Psi = \rho\left(\frac{\partial c^2}{\partial p}\right)_\rho = \gamma_{pv} + \left(\frac{\partial \gamma_{pv}}{\partial p}\right)_\rho p$	γ

maximum value of corrected mass flow per unit area at choking conditions decreases with increasing values of γ_{pv}.

Other studies investigated dense vapor effects in physical processes using one-dimensional theory with either constant energy transfer as heat or wall friction. These are often labeled as *Rayleigh* and *Fanno* flows, respectively; Anderson,[35] Chap. 3, provides a complete analysis of both processes under the perfect gas assumption. Following the approach of Schnerr and Leidner,[36] Cramer provided a qualitative analysis of Fanno[37] and Rayleigh[38] flows in dense vapors, with a focus on BZT fluids. For his analysis, he adopted the van der Waals fluid thermodynamic model. He proved that as many as three sonic points may occur in Rayleigh processes, while in Fanno flows as many as three sonic points corresponding to two maxima and one minimum in entropy may occur. However, the use of a thermodynamic model based on the van der Waals equation of state leads one to substantially overestimate the extent of the $\Gamma < 0$ region. Furthermore, non-classical gasdynamic studies are still purely theoretical in nature, and applications have not been devised yet. On the contrary, non-ideal flows occurring with the fluid in states characterized by $0 < \Gamma < 1$ are of relevant industrial interest. Characterizing the influence of non-ideal fluid dynamics on relevant turbulent viscous and diabatic processes becomes thus of prime importance to correctly predict the performance of internal flow devices. However, a quantitative understanding of the impact of the fluid state on both viscous turbulent and diabatic processes is scarcely documented in the literature.

The aim of this study is to evaluate the impact of both fluid molecular complexity and thermodynamic non-ideality on some paradigmatic compressible non-ideal flow processes, using state-of-the-art fluid thermophysical models. Loss mechanisms and relevant trends in flow variables are both qualitatively and quantitatively estimated.

The article is structured as follows. Section II lists the characteristic non-dimensional fluid parameters used in this study and discusses the importance of the Grüneisen parameter which is used here for the first time in relation to molecular complexity. In Sec. III, a general theoretical framework for one-dimensional compressible flows is derived from first-principle equations; here, the parameters introduced in Sec. II are used to characterize these flows. The obtained framework can be used for preliminary investigations of loss mechanisms affecting the performance and operation of turbomachinery, heat exchangers and in other engineering applications. Section IV treats the impact of the fluid, namely, of its molecules, on chocking and the trend of flow variables in channel flows with constant thermal energy addition (Rayleigh flow) and wall friction (Fanno flow). In addition, the friction coefficient in turbulent channel flows of dense vapors is estimated with three-dimensional Reynolds Averaged Navier–Stokes simulations (RANS) of pipe flows and compared with values resulting from the friction coefficient formulation valid for incompressible flows. Section V describes the impact of the fluid and its properties on two paradigmatic one-dimensional mixing flow configurations, namely, the mixing of two streams and flow injection. Section VI outlines the main conclusions drawn from this study.

II. NON-DIMENSIONAL FLUID PROPERTIES CHARACTERIZING DENSE VAPORS

The ideal gas equation of state reads

$$p = \rho R T. \tag{3}$$

If Eq. (3) holds, then $Z = 1$. Fluid states close to the critical point or close to the dew line do not obey the ideal gas law, see Fig. 1. The isobaric and isochoric heat capacity, their ratio $\gamma = c_p/c_v$, and Z vary depending on the fluid state, see Reynolds and Colonna,[39] Chap. 6. The principle of corresponding states is based on the observation that, at fixed reduced temperature and pressure, different fluids have, to a certain degree of approximation, the same value of Z, see Reynolds and Colonna,[39] Fig. 6.6. Therefore, Z is a thermodynamic similarity parameter that is also useful for fluid dynamic analyses.

However, fluid-dynamic processes can be better examined by using other dimensionless state properties. Isentropic flows of dense vapors are described by the thermodynamic relation

$$p/\rho^{\gamma_{pv}} = \text{const.}, \tag{4}$$

in analogy with isentropic flows of fluids in the ideal gas state.[40] Figure 1 shows the variation of γ_{pv} in the temperature-entropy diagram for fluids made with molecules of different degree of complexity.

Differentiation of Eq. (4) yields[41]

$$\gamma_{pv} = -\frac{v}{p}\left(\frac{\partial p}{\partial v}\right)_s = -\gamma\frac{v}{p}\left(\frac{\partial p}{\partial v}\right)_T = \frac{\gamma}{\beta_T p}, \tag{5}$$

where β_T is the isothermal compressibility of the fluid, whose definition is reported in Table I. Both β_T and γ are positive for all fluids in the vapor state; as a consequence, $\gamma_{pv} > 0$ for all fluid thermodynamic states. Differentiating Eq. (5) with respect to the specific volume leads to

$$\Gamma = \frac{1}{2}\left[\gamma_{pv} + 1 - \frac{v}{\gamma_{pv}}\left(\frac{\partial \gamma_{pv}}{\partial v}\right)_s\right]. \tag{6}$$

For flows with moderate variations of thermodynamic properties, the approximation $\Gamma \simeq (\gamma_{pv} + 1)/2$ holds, therefore, $\gamma_{pv} \approx$ const.. This relation is similar to the relation valid for the ideal gas, see Eq. (2).

If an isentropic process is considered and temperature and pressure are taken as primary variables, the governing law becomes

$$Tp^{\gamma_{pT}} = \text{const.}. \tag{7}$$

Its differentiation[41] yields

$$\gamma_{pT} = \frac{p}{T}\left(\frac{\partial T}{\partial p}\right)_s = \frac{\gamma - 1}{\gamma}\frac{\beta_T p}{\beta_p T}, \tag{8}$$

where γ_{pT} is the so-called isentropic pressure–temperature exponent, and β_p is the isobaric compressibility of the fluid. The derivation is provided in Appendix A.

In addition to the fundamental derivative Γ, an additional non-dimensional parameter is required to evaluate the variation of the speed of sound in non-isentropic processes, see Appendix B. This parameter is defined as

$$\Psi \equiv \rho\left(\frac{\partial c^2}{\partial p}\right)_\rho = \gamma_{pv} + \left(\frac{\partial \gamma_{pv}}{\partial p}\right)_\rho p. \tag{9}$$

The second expression in Eq. (9) (see Appendix A) highlights that Ψ is directly linked to the variation of γ_{pv} with pressure over an isochoric process. The term $(\partial\gamma_{pv}/\partial p)_\rho p$ is negative for fluids characterized by low complexity of the molecular structure in thermodynamic regions where $\rho > \rho_{cr}$ and $T \simeq T_{cr}$. However, in these cases, the absolute value of this term never exceeds the one of γ_{pv}; as a consequence $\Psi > 0$ in the vapor region for all fluids. As discussed in Sec. IV, Ψ affects the variation of the Mach number in both Rayleigh and Fanno flows.

Finally, the Grüneisen parameter for fluids is defined as[42]

$$G \equiv \frac{1}{\rho c_v}\left(\frac{\partial p}{\partial T}\right)_v. \tag{10}$$

The Grüneisen parameter is commonly used in equations of state for solids to relate thermodynamic variables with the lattice vibrational spectra. In particular, Eq. (10) provides the average over the values of Grüneisen parameter calculated for each individual mode of the lattice vibrational spectrum of the solid.[43] This parameter is often assumed to be constant with temperature in solids. Arp *et al.*[42] generalized the definition provided by Eq. (10) to fluid phases. Using the Maxwell thermodynamic relations[39] and Eqs. (5), (A10), and (A11), the Grüneisen parameter can also be written as

$$\begin{aligned} G &= -\frac{v}{c_v}\left(\frac{\partial s}{\partial v}\right)_T = \frac{v}{c_v}\frac{(\partial s/\partial p)_T}{(\partial v/\partial p)_T} = -\frac{v}{c_v}\frac{(\partial v/\partial T)_p}{(\partial v/\partial p)_T} \\ &= \frac{v}{c_v}\frac{\beta_p}{\beta_T} = \frac{\gamma - 1}{\beta_p T} = \gamma_{pv}\gamma_{pT}. \end{aligned} \tag{11}$$

The use of the Grüneisen parameter in fluid dynamics theory is quite limited,[44,45] and systematic studies involving G are limited to liquid flows.[46,47] Recently, Mausbach *et al.*[43] examined the variation of the Grüneisen parameter over the temperature-entropy diagram for 28 pure fluids. Estimations of the value of G based on molecular simulations are compared against the values obtained with state-of-the-art multiparameter equations of state models. The results showed that the Grüneisen parameter for vapor states increases with the density and decreases with the temperature for all the examined pure fluids, with the exception of water.

In general, fluids can be classified depending on the level of complexity of their molecules. A parameter for the evaluation of molecular complexity has been defined differently by different authors. Bethe[16] first proposed

$$\delta_\infty^c = \frac{R}{c_{v\infty}(T_c)}. \tag{12}$$

$c_{v\infty}$ is defined as the isochoric specific heat evaluated at the critical temperature T_c in the limit $v \to \infty$. Guardone and Argrow[48] concluded, based on an analysis conducted on selected BZT fluorocarbons, that dense-vapor effects are strongly influenced by δ_∞^c and by the acentric factor of the molecule. The authors also proved that, if the van der Waals and the Redlich–Kwong equations of state models are employed, the minimum values of the fundamental derivative of gas dynamics evaluated along both the critical isotherm and the saturation curve are monotonically increasing functions of δ_∞^c for the selected fluorocarbons. The minimum value of the fundamental derivative Γ_{min} along the vapor–liquid equilibrium curve is thus adopted in subsequent studies by the same group to classify the molecular complexity of fluids.[28] Using a thermodynamic approach based on the simple van der Waals model, Colonna and Guardone[49] and Harinck *et al.*[50] explained the link between the value of δ_∞^c and molecular complexity from a physical point of view. According to the energy equipartition principle, the number of active degrees of freedom of the molecule evaluated at the critical temperature $N(T_c)$ is given by

$$N(T_c) = \frac{2}{\delta_\infty^c}. \tag{13}$$

As a result, the molecular complexity does not depend on molecular weight. Furthermore, the trend of δ_∞^c with the molar mass is strictly monotone if the considered fluids belong to the same class (e.g., hydrocarbons, siloxanes, or fluorocarbons), therefore, have similar molecular structures.

In the ideal gas limit, δ_∞^c tends to the value of the inverse of the Grüneisen parameter evaluated at the critical temperature: combining Eq. (10) with $p = \rho ZRT$ yields

$$G = \frac{1}{\delta_\infty^c}\frac{c_{v\infty}}{c_v}\left[Z + T\left(\frac{\partial Z}{\partial T}\right)_\rho\right]. \tag{14}$$

In this equation, δ_∞^c accounts for the molecular complexity of the fluid, while the remaining terms account for its departure from the ideal gas value. In the dilute gas region, $Z \to 1$, $c_v \to c_{v\infty}$ and the derivative of Z vanishes, therefore, $G_\infty \to 1/\delta_\infty^c$, where G_∞ denotes the Grüneisen parameter evaluated according to the ideal gas assumption and along the critical isotherm.

In process and energy engineering, given that also processes entailing phase change are of interest, the molecular complexity of the working fluid is often evaluated by means of the coefficient σ, defined as[52]

$$\sigma = \frac{T_{cr}}{R}\left(\frac{\mathrm{d}s}{\mathrm{d}T}\right)_{\text{sat},T_r=0.7} = \frac{1}{0.7R}\left[\frac{(\gamma-1)}{G^2}\gamma_{pv}ZR - \frac{\gamma-1}{G}\frac{1}{\rho}\frac{\mathrm{d}p_{\text{sat}}}{\mathrm{d}T}\right]_{\text{sat},T_r=0.7}, \tag{15}$$

where the subscript sat denotes dew point variables, and $T_r = 0.7$ means that the saturated property is evaluated for a temperature that

is 0.7 times the critical value. Equation (15) highlights the link between σ and some fluid parameters. The σ coefficient is proportional to the slope of the dew line of the fluid in the Ts diagram, which is primarily a function of the heat capacity of the saturated vapor. Charts in Invernizzi,[52] Sec. 2.5, show that σ increases with the molecular complexity of the fluid. In particular, the slope of the dew line in the temperature entropy diagram, and thus σ, is positive for fluids with a high molecular complexity. Conversely, σ is negative for fluids characterized by a simple molecular structure.

The graph in Fig. 2(a) can be used to compare the various definitions of molecular complexity with the aim of evaluating which parameter best fits results for a large number of fluids representative of a wide range of molecular complexities. All values are evaluated using multiparameter equations of state models for a number of fluids for which input data are available and that are implemented in a well-known commercial program.[51] Data of σ and the inverse of G_∞ (and thus δ^c_∞) are fitted with a linear regression. A third-order polynomial function is instead used to fit $1/(\Gamma_{min}+1)$ with σ. Unity is added to the denominator to attain a smooth and monotone fit of the data also in case some BZT fluids characterized by $\Gamma_{min}<0$ are included in the analysis. The maximum deviations between the calculated $1/G_\infty$ and the linearly interpolated values occur for $\sigma<0$ and $\sigma>80$. The deviations between the calculated $1/(\Gamma_{min}+1)$ values from their polynomial fit are considerably larger (>500%) for large values of molecular complexity, while they are smaller for low values.

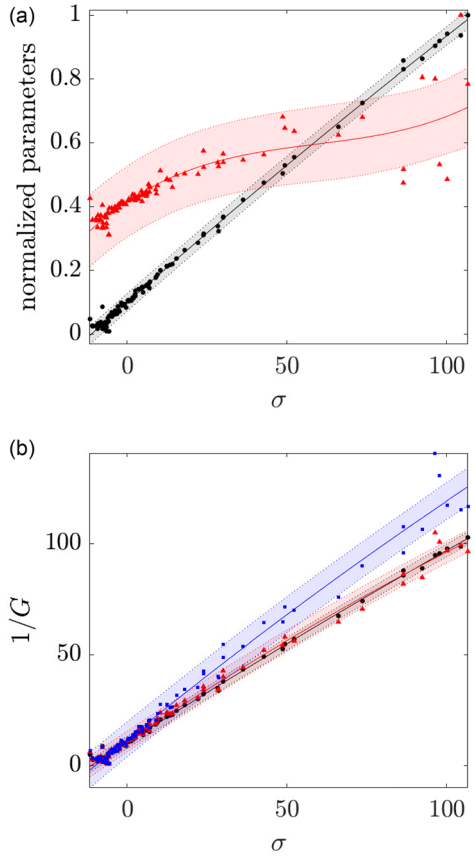

FIG. 2. Fluid thermodynamic parameters that were defined to evaluate the molecular complexity in previous studies (Γ_{min} and σ) and their relation with the Grüneisen parameter. All values are calculated with the multiparameter equation of state models implemented in a well-known property estimation program.[51] (a) Variation of black dot $1/G_\infty=\delta^c_\infty$ and red triangle $1/(\Gamma_{min}+1)$ with σ. $1/G_\infty$ is normalized with $1/G_{\infty,min}=107.92$, while $1/(\Gamma_{min}+1)$ is normalized with $1/(\Gamma_{min}+1)_{min}=1.29$ (b) Grüneisen parameter vs σ as a function of several values of reduced temperature and pressure. Black dot $T_r=0.9$; $p_r=0.05$, red triangle $T_r=1$; $p_r=0.65$, blue square $T_r=1$; $p_r=0.85$. Linear regression fitting curves are also reported as solid lines with their respective 95% confidence bounds (shaded areas).

Figure 2(b) shows the relation σ vs $(1/G)$ for three different sets of reduced temperatures and pressures and for the same fluids considered in Fig. 2(a). The results prove that the linear relation between σ and $1/G$ is maintained, albeit less rigorously, also in the dense vapor region: substantial deviations from the linear relation between σ and $1/G$ can be observed only in the case $T_r=1, p_r=0.85$. G can, therefore, be used to quantify the complexity of pure fluid molecules and as non-dimensional property for the comparison of flow processes featuring different working fluids.

Graphs in Fig. 3 show the variation of each fluid parameter along the critical isotherm at $p<p_c$. Four different fluids of different molecular complexity are reported. Regardless of their molecular complexity, the specific heat ratio γ and the inverse of the compressibility factor Z increase monotonically with the reduced pressure p/p_{cr}. For values of pressure approaching that of the critical point, the value of γ increases more sharply, more so for simple molecules. For low molecular complexity fluids, the Grüneisen parameter peaks in proximity of the critical point and converges to the ideal gas value as the pressure decreases. However, for fluids made of increasingly complex molecules [Figs. 3(c) and 3(d)], the ratio G/G_∞ is a monotonic function of the pressure; thus, no maximum value exists. The trend of the function Ψ/Ψ_∞ is opposite to that of G/G_∞. The parameter which is mostly affected by molecular complexity is the generalized isentropic exponent γ_{pv}. For low values of molecular complexity [Fig. 3(a)], γ_{pv} monotonically increases with pressure and tends to a finite value at the critical point. For moderate molecular complexity values [Fig. 3(b)], the $\gamma_{pv}/\gamma_{pv,\infty}$ function exhibits a minimum value, while for fluids made of the complex molecules [Figs. 3(c) and 3(d)], the trend is monotone. Notably, $\gamma_{pv}<1$ for states in the superheated vapor region of molecularly complex substances [see Fig. 1(b)]. Finally, the fundamental derivative of gas dynamics monotonically increases with pressure in fluids with a low molecular complexity. For fluids made of increasingly complex molecules [Figs. 3(c) and 3(d)], the function Γ/Γ_∞ exhibits a minimum in proximity of the critical point.

Summarizing, all non-dimensional fluid properties carry information about the relevance of thermodynamic non-ideality of fluids. Nevertheless, depending on the type of analysis or application, one parameter can be more suited than the others. For example, the compressibility factor Z can be effectively used to ensure thermodynamic similarity between physical processes occurring in different fluids. The exponent γ_{pv}, instead, has recently been utilized to assess the impact of fluid non-ideality on the design of turbomachinery components. The design of turbine nozzles for ORC systems operating with dense vapors strongly depends on the value of γ_{pv}.[53] The value of the fundamental derivative of gas dynamics Γ is paramount for assessing dense vapor effects in relation to the propagation of waves in fluids. It can, therefore, be argued that the Grüneisen parameter is particularly suitable for the

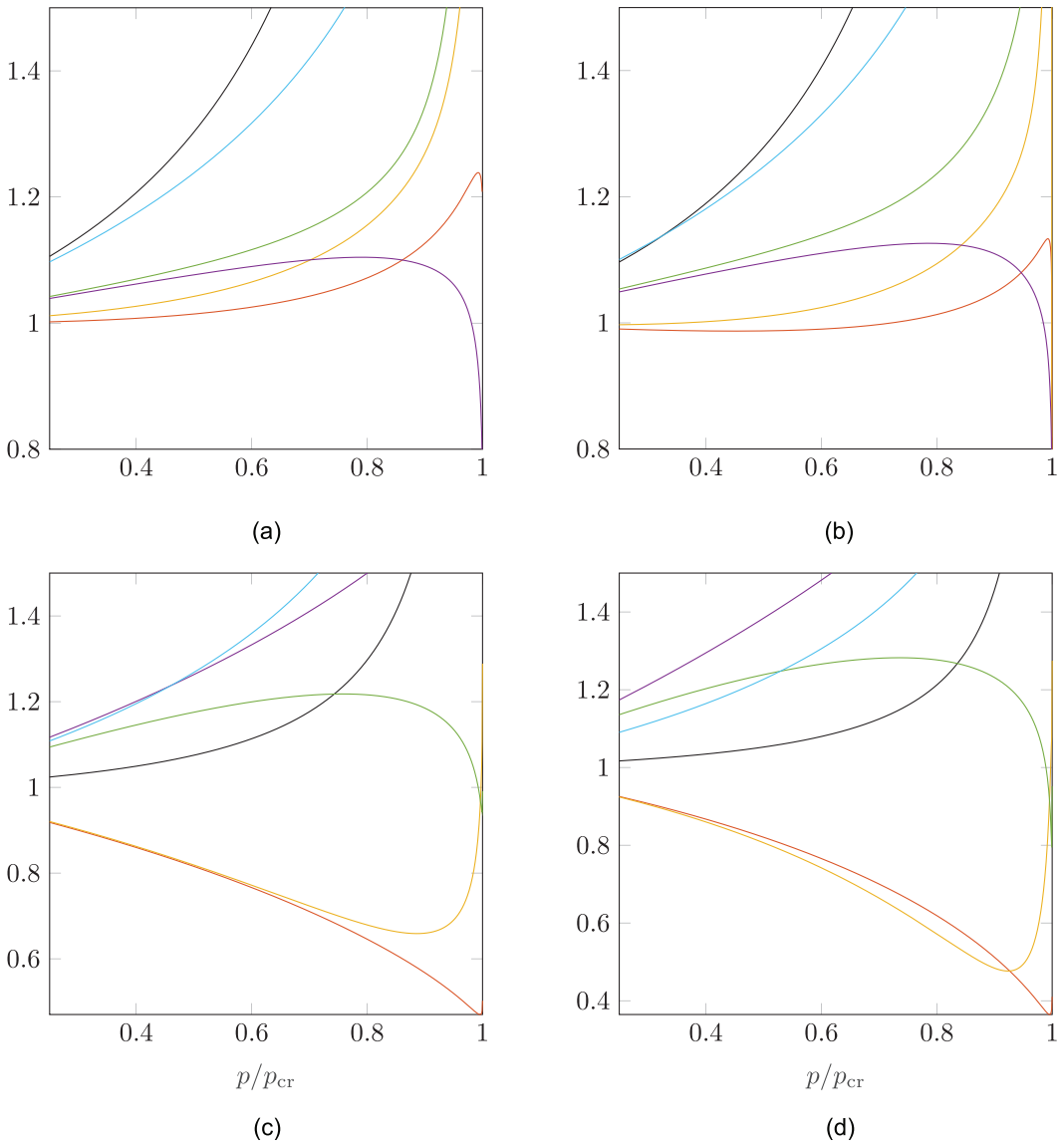

FIG. 3. Variation of fluid properties along the critical isotherm for several fluids, where ∞ denotes the properties estimated at $v \to \infty$. (a) nitrogen, (b) CO_2, (c) toluene, and (d) siloxane MM. Fluid parameters: Black line γ/γ_∞, blue line $\gamma_{pv}/\gamma_{pv,\infty}$, orange line Γ/Γ_∞, yellow line G/G_∞, purple line Ψ/Ψ_∞, and green line $1/Z$.

study of the role of fluid molecular complexity if paradigmatic non-reactive flows of pure fluids and mixtures are considered.

III. THEORETICAL FRAMEWORK

The derivation of the one-dimensional theoretical framework for the analysis of paradigmatic flows of dense vapors is based on the work of Shapiro,[54] which is limited to ideal gas flows. This analysis was later further elaborated by Greitzer *et al.*[55] Arp *et al.*[42] and, more recently, Baltadjiev *et al.*[11] extended part of Shapiro's framework to the case of dense vapor flows, in which the fluid thermodynamic properties are obtained with an arbitrary equation of state model. This framework is extended here to the case of non-isentropic processes, and the fluid parameters introduced in Sec. II are used to quantify the influence of both the molecular complexity of the working fluid and the thermodynamic operating conditions.

The differential conservation equations for an infinitesimal control volume [see Fig. 4(a)] with a variable cross-sectional area A, frictional wall stresses τ_w, infinitesimal energy transfer as shaft work to the fluid dw_{shaft}, and as heat to the fluid dq, and mass flow injection $d\dot{m}$ read[55]

$$\frac{d\rho}{\rho} + \frac{du}{u} + \frac{dA}{A} = 0, \tag{16}$$

$$\rho u A du + A dp = -\rho A dw_{shaft} - \tau_w dA_w + d\dot{m}(u_{inj}\cos\alpha - u), \tag{17}$$

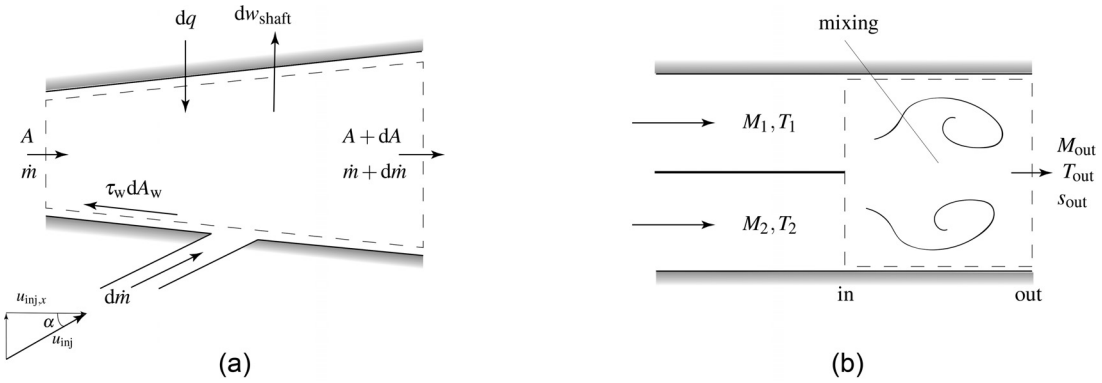

FIG. 4. (a) Control volume for the analysis of one-dimensional compressible flows with a variable cross-sectional area, energy transfer as heat or shaft work, wall friction, and fluid injection. (b) Mixing of two co-flowing streams in a constant area channel. The dashed lines identify the control volume used for the mixing loss calculation.

$$\begin{aligned} \mathrm{d}h_\mathrm{t} &= \mathrm{d}h + u\mathrm{d}u + \left[h_\mathrm{inj} - h_\mathrm{inj,in} + \frac{u^2}{2} - \frac{u_\mathrm{inj}^2}{2}\right]\frac{\mathrm{d}\dot{m}}{\dot{m}} \\ &= \mathrm{d}q - \mathrm{d}w_\mathrm{shaft}, \end{aligned} \tag{18}$$

where u is the absolute flow velocity, ρ the density, A the cross-sectional area, p the pressure, A_w the wetted surface area around the control volume, u_inj the velocity of the injected mass flow, α the mass flow injection angle, and $h_\mathrm{inj,in} = h_\mathrm{inj}(T_\mathrm{inj}, p_\mathrm{inj})$ and $h_\mathrm{inj} = h_\mathrm{inj}(T, p)$ the specific static enthalpy of the injected fluid at the inlet and the outlet of the control volume, respectively.

The arbitrary equation of state in the volumetric form $p = \rho ZRT$ together with the calorimetric equation of state $h = h(T, p)$, forming the thermodynamic model, close the set of equations. The thermodynamic relations $s = s(T, p)$ and $c = c(\rho, s)$ allow one to derive the equations in the desired form.

The system of equations can be manipulated to obtain the analytical relations between the infinitesimal variation of each flow quantity, for instance, pressure or temperature, and the variation of cross-sectional area, the energy transfer as heat, the shaft work, and the wall friction. The contribution due to the injected mass flow is neglected, and it is separately analyzed in Sec. V. With this approach, one can analyze the influence of the non-ideality of the fluid properties on the variation of each flow quantity for a given change of cross-sectional area, energy transfer as heat and shaft work, and wall friction. Table II lists all these relations, whose derivation is reported in Appendix B. All the relations can be formalized in the synthetic form

TABLE II. Influence coefficients for compressible channel flow and real gas in terms of γ, Γ, G, γ_{pv}, and Ψ.

	$\frac{\mathrm{d}A}{A}$	$\frac{-\mathrm{d}q}{c_pT}$	$\frac{-\mathrm{d}w_\mathrm{shaft}}{c_pT}$	$4C_f\frac{\mathrm{d}x}{d_H}$
$\frac{\mathrm{d}\rho}{\rho}$	$\frac{M^2}{1-M^2}$	$-\frac{(\gamma-1)}{G}\frac{1}{1-M^2}$	$-\frac{(\gamma-1)}{G^2}\frac{1}{1-M^2}$	$-\frac{G+1}{2}\frac{M^2}{1-M^2}$
$\frac{\mathrm{d}p}{p}$	$\frac{\gamma_{pv}M^2}{(1-M^2)}$	$-\frac{\gamma_{pv}(\gamma-1)M^2}{G(1-M^2)}$	$-\frac{\gamma_{pv}(\gamma-1)}{G^2(1-M^2)}$	$-\frac{\gamma_{pv}M^2}{2}\frac{1+GM^2}{1-M^2}$
$\frac{\mathrm{d}T}{T}$	$\frac{GM^2}{1-M^2}$	$-\frac{\gamma M^2-1}{1-M^2}$	$-\frac{(\gamma-1)}{G(1-M^2)}$	$-\frac{G\left[(\gamma M^2-1)G+(\gamma-1)\right]}{(\gamma-1)(1-M^2)}\frac{M^2}{2}$
$\frac{\mathrm{d}M}{M}$	$-\frac{1+(\Gamma-1)M^2}{1-M^2}$	$\frac{(\gamma-1)}{G}\left[\frac{\Gamma}{1-M^2}-\frac{\Psi}{2}\right]$	$\frac{(\gamma-1)}{G^2}\frac{\Gamma}{1-M^2}$	$\left[\frac{(G+1)\Gamma}{(1-M^2)}-G\frac{\Psi}{2}\right]\frac{M^2}{2}$
$\frac{\mathrm{d}u}{u}$	$-\frac{1}{1-M^2}$	$\frac{(\gamma-1)}{G}\frac{1}{1-M^2}$	$\frac{(\gamma-1)}{G^2}\frac{1}{1-M^2}$	$\frac{G+1}{2}\frac{M^2}{1-M^2}$
$\frac{\mathrm{d}c}{c}$	$\frac{(\Gamma-1)M^2}{1-M^2}$	$-\frac{(\gamma-1)}{G}\left[\frac{(\Gamma-1)}{1-M^2}-\frac{\Psi}{2}\right]$	$-\frac{(\gamma-1)}{G^2}\frac{\Gamma-1}{1-M^2}$	$-\left[\frac{(G+1)(\Gamma-1)}{(1-M^2)}-G\frac{\Psi}{2}\right]\frac{M^2}{2}$
$\frac{\mathrm{d}s}{c_p}$	0	1	0	$\frac{G^2}{\gamma-1}\frac{M^2}{2}$
$\frac{\mathrm{d}h}{c_pT}$	$\frac{G^2}{\gamma-1}\frac{M^2}{1-M^2}$	$-\frac{M^2(G+1)-1}{(1-M^2)}$	$-\frac{1}{1-M^2}$	$-\frac{G^2(G+1)}{(\gamma-1)(1-M^2)}\frac{M^4}{2}$

$$\left.\begin{aligned}\Phi &= f_1\left(\frac{dA}{A}\right) + f_2\left(\frac{-dq}{c_p T}\right) + f_3\left(\frac{-dw_{shaft}}{c_p T}\right) + f_4\left(4C_f \frac{dx}{d_H}\right),\\ f_i &= f_i(\gamma, \gamma_{pv}, \Gamma, G, \Psi, M), \quad i = 1, \ldots, 4,\end{aligned}\right\} \tag{19}$$

where Φ is the normalized differential variation of a thermodynamic or fluid dynamic variable, e.g., temperature or flow velocity, C_f is the Fanning friction factor, and d_H is the hydraulic diameter. The f_i factors are termed *influence coefficients*[54] and solely depend on the Mach number and on some of the non-dimensional fluid properties introduced in Sec. II. As a result, each of the flow quantities in the first column listed in Table II is given by the summation of the product between each independent variable in the first row and the corresponding influence coefficient.

A. Validation: Flow expansion in a convergent–divergent nozzle

This case has already been treated extensively in the literature; here, only a comparison with recent experimental data obtained with a blow-down wind tunnel realizing the supersonic expansion of octamethyltrisiloxane (siloxane MDM) is reported. The accuracy of the one-dimensional framework has been quantitatively verified by comparing the values of Mach number and static pressure along the channel calculated with the equations of Table II against the experimental values documented in Spinelli *et al.*[56] Figure 5 shows the comparison between these experimental data and the values obtained with the one-dimensional model valid for dense vapors and that valid for the ideal gas, see Anderson,[35] Chap. 3. The governing flow equations were discretized with a first-order Euler scheme in space and solved numerically. Boundary conditions in terms of inlet total pressure, total temperature, and Mach number were prescribed so that they matched the corresponding experimental values. Table III reports the main data identifying the four test cases considered in this analysis. Two different convergent– divergent nozzle geometries are considered for the cases termed M1.5H, M1.5L and M2.0L, M2.0H by Spinelli *et al.*[56] Fluid properties of MDM are evaluated using the state-of-the-art multiparameter equation of state model by Thol *et al.*[57] The experimental data are those acquired at $t = 0$ s, i.e., immediately after the opening of the main control valve.

With reference to Fig. 5, the pressures calculated with dense-vapor flow model match the experimental data with acceptable accuracy considering the limitations of the model: the relative difference between values obtained with the numerical model and values obtained from measurements never exceeds 6.5% for all cases. Mach numbers calculated with the one-dimensional model feature values that are within the uncertainty band associated with the experimental data. The values of pressure and Mach number computed with ideal gas model are rather accurate if the inlet pressure is low, i.e., for the M1.5L and M2.0L test cases. The ideal gas model predictions are increasingly inaccurate with higher inlet pressures, as far as the values related to the divergent part of the nozzle are concerned ($Z_t \sim 0.65$ at the nozzle inlet). The discrepancy between the outlet static pressure calculated with the dense-vapor model and the ideal gas model is ∼12% for both cases M1.5H and M2.0H and ∼6% for the remaining cases.

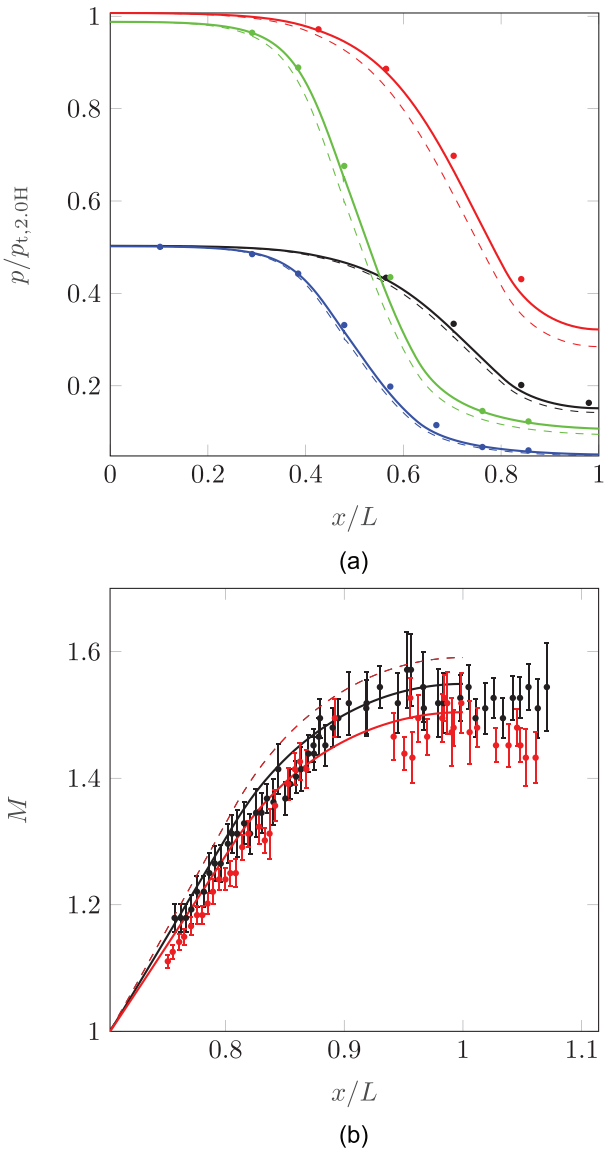

FIG. 5. Validation of the one-dimensional equations for an isentropic vapor flow through a supersonic nozzle by comparison with the measurements (Spinelli *et al.*[56]). The working fluid is siloxane MDM. The results of the calculations performed by assuming that the fluid obeys the ideal gas law are also reported. (a) Pressure vs axial coordinate. (b) Mach number vs axial coordinate. For both graphs: ——: fluid properties calculated with a multiparameter equation of state model,[57] – – –: fluid properties calculated with the ideal gas model, dot: measured values (pressure) or values derived from measured information (Mach) with corresponding error bars; cases, as termed by Spinelli *et al.*:[56] black line: M1.5L, red line: M1.5H, blue line: M2.0L, and green line: M2.0H.

IV. PARADIGMATIC ONE-DIMENSIONAL COMPRESSIBLE FLOWS OF DENSE VAPORS

The influence coefficients $-dq/(c_p T)$ and $4C_f dx/d_H$ reported in Table II are instrumental to the analysis of Rayleigh and Fanno processes in dense vapors. These configurations are representative of

TABLE III. Several flow properties identifying the inlet conditions of the selected test cases treated in Spinelli *et al.*[56] The total compressibility factor Z_t is calculated starting from the inlet total quantities.

Test	p_t (bar)	T_t (K)	$p_{r,t}$	$T_{r,t}$	Z_t
M1.5L	4.59	512.15	0.32	0.91	0.81
M1.5H	9.20	541.15	0.64	0.96	0.63
M2.0L	4.58	520.15	0.32	0.92	0.82
M2.0H	9.02	542.15	0.63	0.96	0.65

actual flow processes in engineering applications. On the one hand, non-adiabatic flows can be encountered, for example, in small-scale turbines for ORC systems and heat exchangers. Moreover, the Rayleigh flow simplification can be adopted for the preliminary assessment of supercritical injection processes in combustors. On the other hand, profile losses due to the presence of a laminar or turbulent boundary layer on blade surfaces and contributing to the total loss in turbomachinery can be modeled by means of the Fanno flow.[13] To the authors' knowledge, no study on the influence of the fluid on each of these paradigmatic flows in the non-ideal, albeit classical, regime is available in the literature. Only some studies about non-classical flows were carried out in the past,[36–38,42,58] but they are based on the estimation of fluid thermodynamic properties by means of largely inaccurate thermodynamic models, such as the van der Waals equation of state.

For this analysis, equations in Table II are discretized with a first-order forward scheme for an infinitesimal control volume of length dx and numerically integrated over a given length. Non-dimensional fluid parameters are estimated within each infinitesimal control volume as the average of the value calculated at the edge of each control volume. Calculations are performed for nine different fluids (see Table IV) and different inlet conditions. The state-of-the-art multiparameter equations of state models implemented in an in-house software for the calculation of thermophysical properties[51,59] are adopted. To ensure thermodynamic similarity among all the fluids, two sets of inlet conditions in terms of reduced temperature and pressure are considered, namely, those characterized by $T_r = 1.05$, $p_r = 1.15$ and by $T_r = 0.9$, $p_r = 0.05$. The compressibility factor associated with the high-pressure and high-temperature inlet condition is $Z \simeq 0.5$, while that associated with the dilute-gas inlet condition is $Z \simeq 1$. Calculations are stopped either when pressure and temperature equal the corresponding saturated values or the outlet Mach number M_{out} is equal to 1.4. For the majority of the considered fluids, the limit assures that, in the supersonic regime, the thermodynamic model is within its range of validity. The discretization is locally refined in proximity of the sonic point to avoid numerical divergence.

TABLE IV. Fluids adopted for the analysis of Rayleigh and Fanno flows and characteristic properties. The markers in the last column are used in Figs. 6, 7, 11, and 12.

Fluid	M_{mol} (g mol^{-1})	T_{cr} (K)	p_{cr} (bar)	γ_∞	Γ_{min}	G_∞	Marker
N_2	28.01	126.19	33.96	1.40	1.3390	0.40	——
O_2	32.00	154.58	50.43	1.40	1.3314	0.40	- - -
CO_2	44.01	304.13	73.77	1.30	1.1944	0.3004	——
Isobutane	58.12	407.81	36.29	1.08	0.7105	0.0775	- - -
Toluene	92.14	591.75	41.26	1.05	0.5849	0.0486	——
MM	162.38	518.70	19.39	1.03	0.3395	0.0272	- - -

A. Rayleigh flow of dense vapors

Figures 6(a) and 6(b) show the Rayleigh curves evaluated for $Z \simeq 0.5$ and $Z \simeq 1$, respectively. The results are reported for the fluids of Table IV. The inlet Mach number M_{in} is set to 0.7. For each curve, the point at maximum $\Delta s/c_{p,in}$, with $c_{p,in}$ denoting the isobaric specific heat evaluated at the inlet, corresponds to the thermodynamic state where choking occurs. The heat transferred to each infinitesimal control volume is equal to 100 J: this value has been chosen after a sensitivity analysis. To assure a better refinement at $M \simeq 1$, the value of dq is changed by a factor 1.75 every time the value of the first non-decimal unit of the parameter $10 \cdot M$, where M is the flow Mach number, increases of 1.

The use of the appropriate influence coefficients in Table II yields the relation

$$\frac{\mathrm{d}h}{\mathrm{d}q} = \frac{1}{T}\frac{\mathrm{d}h}{\mathrm{d}s} = -\frac{M^2(G+1)-1}{(1-M^2)}. \tag{20}$$

Equation (20) shows that, at fixed reduced inlet temperature and pressure, both the Mach number and the Grüneisen parameter directly affect the variation of the specific enthalpy of the fluid along the duct. In particular, the Grüneisen parameter is related to the slope of the Rayleigh curves: fluids with a higher molecular complexity exhibit a larger enthalpy increase if compared to fluids made of simpler molecules. This shows that, as expected, substances characterized by a low value of G convert into internal energy a larger amount of thermal energy transferred to the flow. Combining the relation $\mathrm{d}u/u = f(\gamma, G, M) \cdot \mathrm{d}q/(c_p T)$, which can be obtained with the influence coefficients of Table II with Eq. (A13), leads to

$$\frac{\mathrm{d}E_k}{\mathrm{d}q} = G\frac{M^2}{1-M^2}, \tag{21}$$

where $E_k = u^2/2$ is the kinetic energy of the fluid. Conversely, substances characterized by high values of G, for instance, nitrogen or oxygen, convert a proportionally larger amount of thermal energy transferred to the flow into kinetic energy. Equation (21) shows that changes in kinetic energy scale linearly with the Grüneisen parameter of the fluid, or, equivalently, are inversely proportional to its molecular complexity. The distribution of the thermal energy input between kinetic and internal energy of the fluid depends on the value of the isobaric specific heat capacity c_p at fixed thermodynamic conditions. From Eqs. (11) and (A12) and the relation $pv = ZRT$, it follows that

$$\frac{c_p}{R} = \frac{(\gamma-1)}{G^2}\gamma_{pv}Z. \tag{22}$$

The factor $1/G^2$ is several orders of magnitude larger than the numerator. As a consequence, the specific heat at constant pressure times the molar mass is inversely proportional to the square of the Grüneisen parameter or, equivalently, directly proportional to the square of the molecular complexity of the fluid. Figures 6(a)–6(c) show that G becomes larger than G_∞ for all the fluids if the fluid state approaches

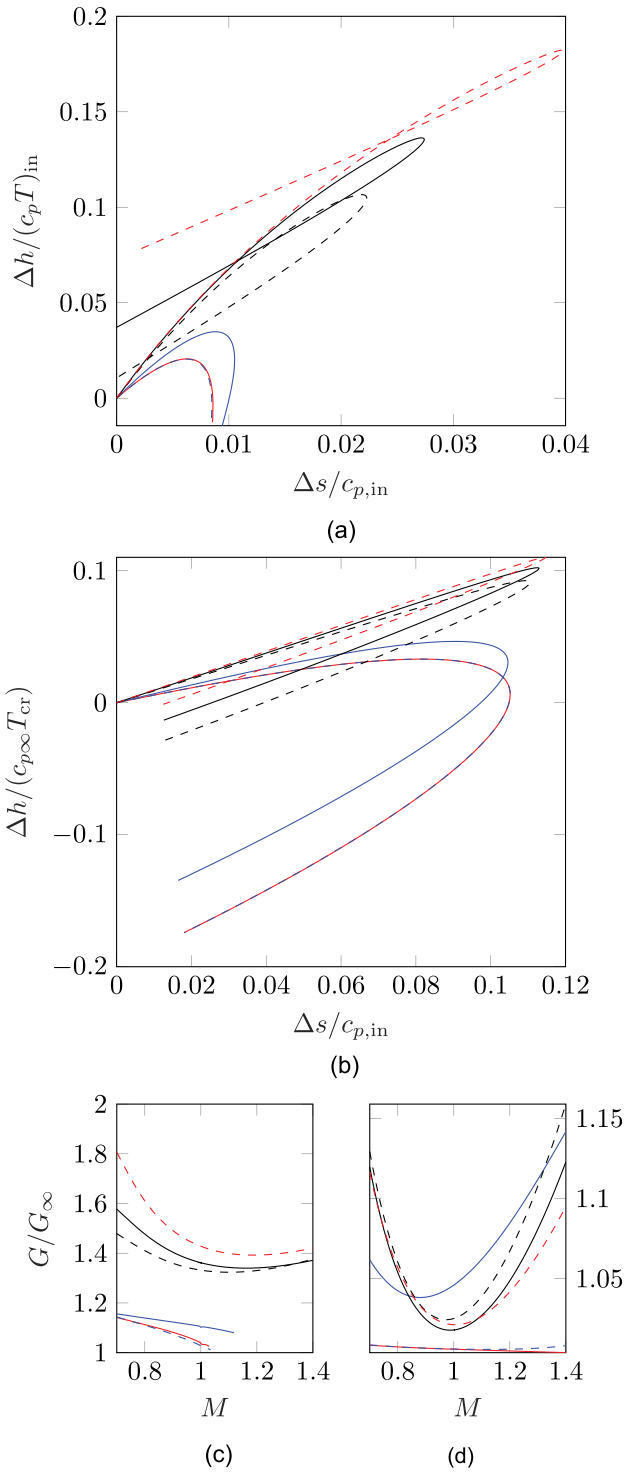

FIG. 6. Rayleigh curves for different fluids at $M_{\rm in} = 0.7$. Markers and colors identifying the curve in relation to each fluid are reported in Table IV. Considered cases: (a) $T_{\rm r} = 1.05$, $p_{\rm r} = 1.15$, $Z \simeq 0.5$; (b) $T_{\rm r} = 0.9$, $p_{\rm r} = 0.05$, $Z \simeq 1$. (c) and (d) report the variation of G/G_∞ for the processes displayed in (a) and (b), respectively.

the critical point of the substance. This results in a steeper enthalpy increase at constant thermal energy input if compared to the case for which $Z \simeq 1$ [Figs. 6(b)–6(d)]. However, this effect is more pronounced for complex molecules, which exhibit a larger deviation of G from the baseline G_∞ value [Figs. 6(c) and 3]. For substances characterized by low values of G_∞, the maximum value of enthalpy along a Rayleigh curve moves closer to the sonic point. Equating to zero Eq. (20) results in

$$M_{\max(h)} = \frac{1}{\sqrt{G+1}}. \tag{23}$$

For complex fluids, $M_{\max(h)} \sim 1$ as $G \to 0$, while $M_{\max(h)} = 1/\sqrt{\gamma}$ for a perfect gas. In other words, adding thermal energy to a subsonic flow of a dense vapor increases the static enthalpy until the choking conditions are reached.

Figures 7(a) and 7(b) show the dimensionless thermal energy flux that is required to choke the flow at different subsonic inlet Mach numbers for both the $Z \simeq 0.5$ [Fig. 7(a)] and the $Z \simeq 1$ [Fig. 7(b)]. Both graphs show that the larger the fluid molecular complexity, the larger the amount of energy that needs to be transferred as heat to the fluid to choke the flow. The influence of the fluid molecular complexity is less visible in the $Z \simeq 1$ case, i.e., if the fluid is in the dilute gas state.

The physical explanation of these results is that fluids made of complex molecules (low values of G_∞), thus with a large number of active molecular degrees of freedom, can store a larger quantity of thermal energy. Therefore, only a small share of the energy transferred as heat contributes to the increase in the kinetic energy of the flow [Eq. (21)]. Note also that the relative amount of thermal energy required to choke the flow starting from subsonic inlet conditions is lower if $Z \simeq 0.5$ compared to the $Z \simeq 1$ case. The difference is larger for simple molecules ($\simeq 10$ times less than the amount evaluated for $Z \simeq 1$). This is due to the higher value of the isobaric specific heat capacity in proximity of the critical point, whose increase is steeper for simple molecules, as it can be inferred from the trend of γ reported in Fig. 3. Similar conclusions for supersonic Rayleigh flows of van der Waals fluids can be found in Schnerr and Leidner.[36]

Figures 8(a) and 8(b) show the variations of Mach number with the normalized entropy increase at different inlet Mach numbers. The results are reported for nitrogen [Fig. 8(a)] and siloxane D_6 [Fig. 8(b)], a BZT fluid. Two sets of inlet temperature and pressure at different levels of thermodynamic non-ideality, namely, $T_{\rm r} = 1$, $p_{\rm r} = 0.9$ and $T_{\rm r} = 0.9$, $p_{\rm r} = 0.05$, are considered. These cases correspond to a value of the compressibility factor at the inlet of $Z \simeq 0.5$ and $Z \simeq 1$, respectively. If the fluid is in the ideal gas state, the Mach number increases monotonically with the entropy, and, consequently, with the energy input as heat. Due to the higher number of molecular degrees of freedom, in Rayleigh flows of fluids made of more complex molecules, like, for instance, siloxane D_6, the Mach number increases less with the input of energy as heat if compared to the Rayleigh flows of simpler molecules.

Figure 8(b) highlights that the trend of Mach number as a function of energy input as heat is non-monotone for subsonic Rayleigh flows of D_6: after an initial decrease, the Mach reaches a minimum and then increases. Solving $\mathrm{d}M/M = f(\mathrm{d}q) = 0$ yields an analytical relation for the inversion of the Mach number, namely,

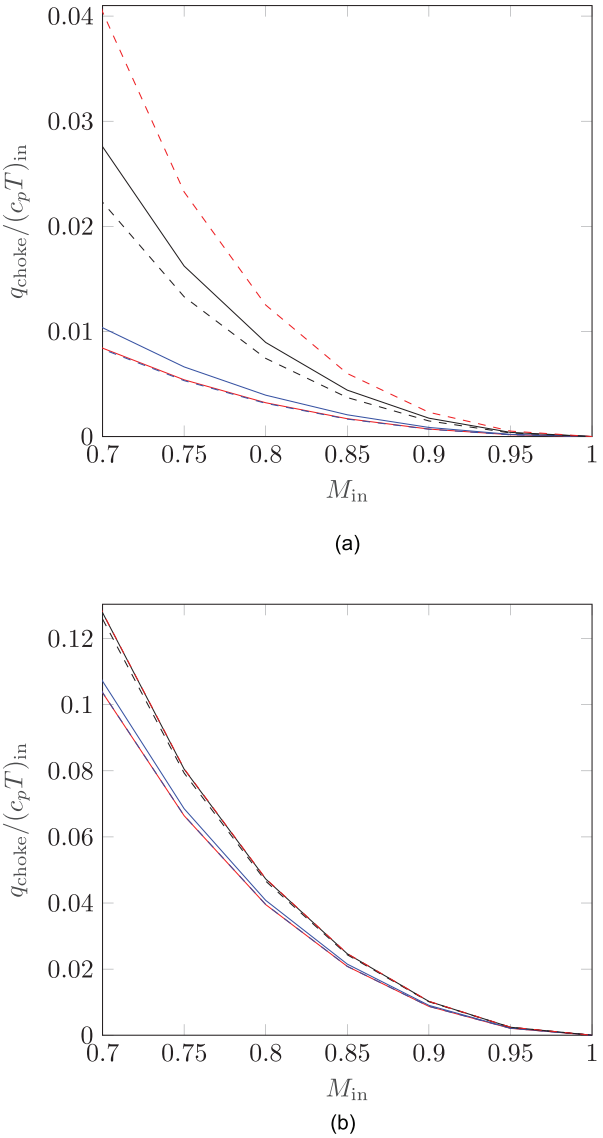

FIG. 7. Non-dimensional energy transfer as heat required to attain choked conditions as a function of the inlet Mach number. Markers and colors identifying the curve in relation to each fluid are reported in Table IV. Considered cases: (a) $T_r = 1.05$, $p_r = 1.15$; and (b) $T_r = 0.9$, $p_r = 0.05$.

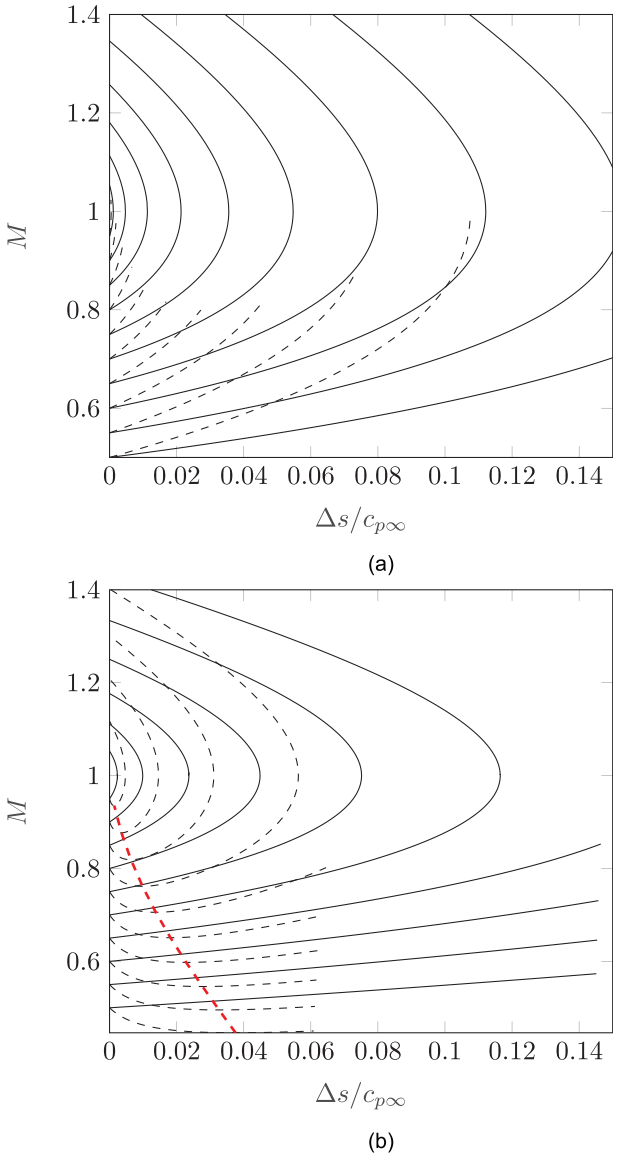

FIG. 8. Mach number vs entropy in Rayleigh processes in (a) nitrogen and (b) siloxane D_6 for different inlet Mach numbers. Two sets of inlet reduced temperature and pressures are considered: – – – $T_r = 1$, $p_r = 0.9$; —— $T_r = 0.9$, $p_r = 0.05$. The red line in identifies the locus of M_{min}.

$$M_{\text{min}} = \sqrt{1 - 2\frac{\Gamma}{\Psi}}, \tag{24}$$

which is defined for

$$\Gamma \geq \frac{\Psi}{2}. \tag{25}$$

If the fluid is in the dilute gas state, $Z \to 1$, $2\Gamma/\Psi \to (\gamma+1)/\gamma$, and M_{min} does not admit real solutions. The red line in Fig. 8(b) identifies the locus of M_{min} for different values of the inlet Mach number. Given that Ψ is greater than zero for all vapor thermodynamic states and for all fluids, also several non-BZT fluids exhibit thermodynamic states for which Eq. (25) is satisfied. This non-classical behavior is due to the steep increase in the speed of sound that dense vapors of complex molecules fluids exhibit in proximity of the critical point, which prevails over the flow acceleration for $M_{\text{in}} < 1$.

Figure 9 depicts the boundaries of the thermodynamic region in which the relation (25) holds in the temperature-entropy diagram of different fluids. The BZT region, i.e., the region satisfying the $\Gamma < 0$ condition, is also reported for comparison. Calculations based on state-of-the-art thermophysical models highlighted that fluids with

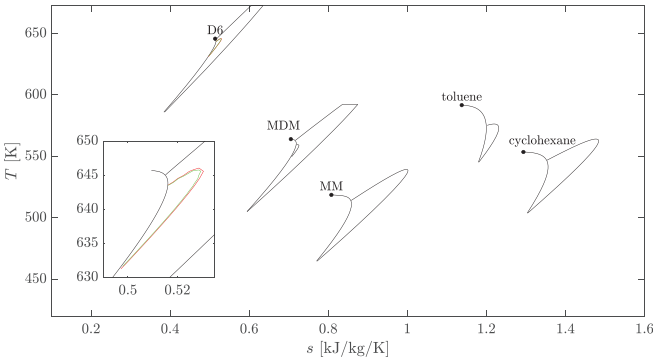

FIG. 9. Boundaries of the thermodynamic regions encompassing states for which $\Gamma < \Psi/2$ in the temperature-entropy diagram for fluids with different molecular complexity. For siloxane D_6, a close-up of the regions in which $\Gamma < \Psi G/[2(G+1)]$ (red) and the $\Gamma < 0$ (green) are also displayed.

$G_\infty < 0.059$ admit a thermodynamic region where the relation (25) is satisfied. Given the small extent of the BZT thermodynamic region of D_6 predicted by current thermodynamic models, the effects on choking as the ones discussed by Cramer[38] and dependent on the van der Waals thermodynamic model are confined to a very restricted range of thermodynamic conditions close to the critical point. Therefore, they are almost impossible to visualize.

B. Fanno flow of dense vapors

Fanno processes have been numerically assessed for all the fluids in Table IV. As shown in Table II, the solution of the one-dimensional equations requires the specification of the friction factor coefficient C_f, which is directly proportional to the entropy generation due to viscous dissipation. Simple algebraic manipulation allows us to write

$$\zeta_s = \int_{s_{in}}^{s_{out}} \frac{T\,\mathrm{d}s}{\frac{1}{2}u^2} = \int_0^L \frac{4C_f\,\mathrm{d}x}{d_H}. \tag{26}$$

Equation (26) shows that the entropy generation due to friction in fully developed channel flows depends on the Fanning friction coefficient and on the pipe aspect ratio L/d_H. Sciacovelli *et al.*[60] recently determined the trend of C_f as a function of the Reynolds number for dense vapors in supersonic fully developed channel flows with isothermal walls by means of direct numerical simulations (DNS). The authors simulated the flows of air and fluorocarbon PP11 ($C_{14}F_{24}$). They estimated the fluid properties using the perfect gas model for air and the Martin–Hou equation state for PP11. The results show that, for dense vapor flows, the dynamic and thermal effects are decoupled to a large extent, and compressibility has a minor effect on the skin friction coefficient if compared to what happens for air flows. Therefore, the skin friction coefficient in dense organic vapor flows tends to the incompressible flow value given by Deans's equation for rectangular duct channels.[61] Numerical simulations of two-dimensional boundary layers with zero pressure gradient conducted by Pini and De Servi[62] further corroborate this finding. However, the study by Sciacovelli[60] has been conducted assuming isothermal channel walls and supersonic flow.

To assess the influence of both flow compressibility and thermodynamic fluid state also for the case of subsonic adiabatic channel flows of dense vapors, three-dimensional axial-symmetric steady-state numerical flow simulations were performed. This study also enabled the assessment of the accuracy of the well-established Colebrook–White empirical model for the computation of the friction factor coefficient in pipe flows.[63] Differently from the approach adopted by Sciacovelli,[60] in this case the Reynolds Averaged Navier–Stokes (RANS) equations model was employed, together with Spalart–Allmaras (SA) turbulence closure model.[64] Despite the accuracy of existing turbulence models for dense vapor flows is not fully ascertained, the work documented in Otero *et al.*[65] proved that eddy viscosity models, such as SA, can provide reasonably accurate values of boundary layer quantities for wall bounded turbulent flows even in the case of strong variations of fluid thermophysical properties. Therefore, the RANS model complemented by the SA eddy viscosity closure is deemed sufficient for the purpose of this analysis. The study described in Sciacovelli *et al.*[66] further corroborates the validity of the approach: the numerical analyses of turbulent channel flows simulated with four variants of the $k-\epsilon$ turbulence model demonstrate that all of the eddy viscosity models provide results that are in qualitative agreement with those obtained with DNS. The considered geometry is a straight 12 m long pipe, limited to a circular sector of 36°. The pipe length was chosen such that fully developed flow is attained for all the case studies. The mesh consists of 1.2×10^6 elements to ensure grid independence. Appendix C reports the results of the grid independence study. The grid is refined in proximity of the wall to ensure accurate resolution of the boundary layer. The first cell height is set to 2×10^{-8} m to guarantee $y^+ < 1$ for all the considered simulations. Rotational periodicity is attained by prescribing symmetry boundary conditions on the remaining interfaces. Flows of two fluids with different level of molecular complexity are investigated, namely, air in ideal gas conditions and siloxane MM. The viscosity value for air is set to 1.831×10^{-5} Pa s over the whole computational domain. Thermophysical properties of siloxane MM are estimated with the state-of-the-art models implemented in a well-known commercial software.[51] Numerical simulations have been performed with a commercial computational fluid dynamic (CFD) software.[67] No-slip and adiabatic conditions are imposed at the smooth wall. Total inlet temperature and pressure are chosen such that the prescribed values of T_r and p_r at the outlet, where the flow is fully developed, are obtained. Table V lists the four considered sets of T_r and p_r at the pipe outlet. These values were set such that the thermodynamic states of the simulated flows are (1) close to vapor–liquid critical state (case Z05 with $Z \simeq 0.5$), (2) in the subcritical and supercritical dense vapor region (cases Z07sub and Z07super, respectively, with $Z \simeq 0.7$) and (3) in the dilute gas state (case Z1 with $Z \simeq 1$). To study the effect of the Mach number on the friction coefficient at the pipe outlet, six values

TABLE V. Values of the outlet reduced temperature and pressure and resulting Mach number range for each of the fluids under investigation.

	T_r	p_r	M range (air)	M range (MM)
Z05	1.05	1.15	0.45–0.69	0.45–0.85
Z07sub	1	0.65	0.43–0.82	0.34–0.79
Z07super	1.1	1.05	0.34–0.72	0.32–0.80
Z1	0.9	0.05	0.6–0.8	0.51–0.83

of normalized pressure difference $(p_{t,in} - p_{out})/L$ are prescribed for each set of T_r and p_r. Table V lists the values of the outlet reduced temperature and pressure for the four different cases, together with the resulting exit Mach number range. In all cases, the value of the Reynolds number calculated with the pipe diameter as reference dimension is sufficiently large to assume fully turbulent flow, i.e., $Re_D = \rho_m u_m D/\mu_{in} > 10^7$, where m stands for *meridional*. In accordance with the observations of Otero *et al.*[65] and Sciacovelli *et al.*,[66] the turbulent Prandtl number is set to 0.9 in all simulations.

Figures 10(a) and 10(b) show the results for air (ideal gas) and siloxane MM. Overall, the values of C_f calculated with the Colebrook–White correlation valid for incompressible flows are larger than the ones obtained from numerical simulations. However, for channel flows with $M < 0.4$ at the outlet, the maximum relative difference between C_f values obtained from CFD simulations and those calculated with the empirical correlation is ∼3%. If $M > 0.4$, for channel flows of air modeled as an ideal gas, C_f values decrease with both M and Re_D, thus deviating from the values calculated with the Colebrook–White correlation. Still in the case of air flows, if $M \simeq 0.7$, the calculated maximum relative difference between C_f values is $\simeq 9\%$ for the Z05, Z07sub, and Z07super cases, and $\simeq 16\%$ for the Z1 case. Conversely, in the case of siloxane MM flows, the C_f vs Re_D curves obtained from CFD simulations follow the same trend given by the Colebrook–White correlation, regardless of the value of M. Therefore, the value of the friction coefficient depends solely on the Reynolds number in the case of flows of low-G fluids and is not influenced by the compressibility of the flow. A low value of the fluid Grüneisen parameter, indeed, implies a low value of the Eckert number of the flow. Simple algebraic manipulation gives

$$Ec = \frac{u^2}{c_p T} = \frac{G^2}{\gamma - 1} M^2, \tag{27}$$

which shows that Ec decreases with the fluid molecular complexity. The lower the Eckert number, the higher the heat capacity of the fluid and the lower the influence of the temperature both on viscous dissipation and on the value of the skin friction. This is in line with results described by Pini and De Servi,[62] who studied dense-vapor effects on the dissipation coefficient C_d in compressible laminar boundary layers. Moreover, these results are also consistent with the outcome of the study of Chen *et al.*,[68] who performed DNS of fully turbulent channel flows and observed that the averaged center-to-wall temperature ratio is lower in the flows of organic fluids with a large molecular complexity and decreases if the fluid state approaches that of the vapor–liquid critical point. Moreover, the Eckert number decreases if the thermodynamic state of the fluid approaches that of the critical point. This is due to the increase in the value of γ, which prevails over that of G, see Fig. 3.

Stemming from these considerations, the Colebrook–White relation is deemed sufficiently accurate for the estimation of the skin friction coefficient in compressible dense vapor flows. Given the lack of correlations for the friction factor coefficient in the case of compressible channel flows of arbitrary fluids, the Colebrook–White equation is also used to estimate C_f for channel flows of high G fluids. In addition, according to Eq. (26), the Colebrook–White equation provides a conservative estimations of the C_f value and, consequently, of the entropy loss coefficient in pipe flows. Furthermore, for subsonic flows, changes of the flow Re_D are more relevant than changes in M. To the authors' best knowledge, the only available correlation for compressible pipe flow is that of Panhandle.[69] However, the validity of the relation is limited to Reynolds numbers between 5×10^6 and 1.4×10^7.

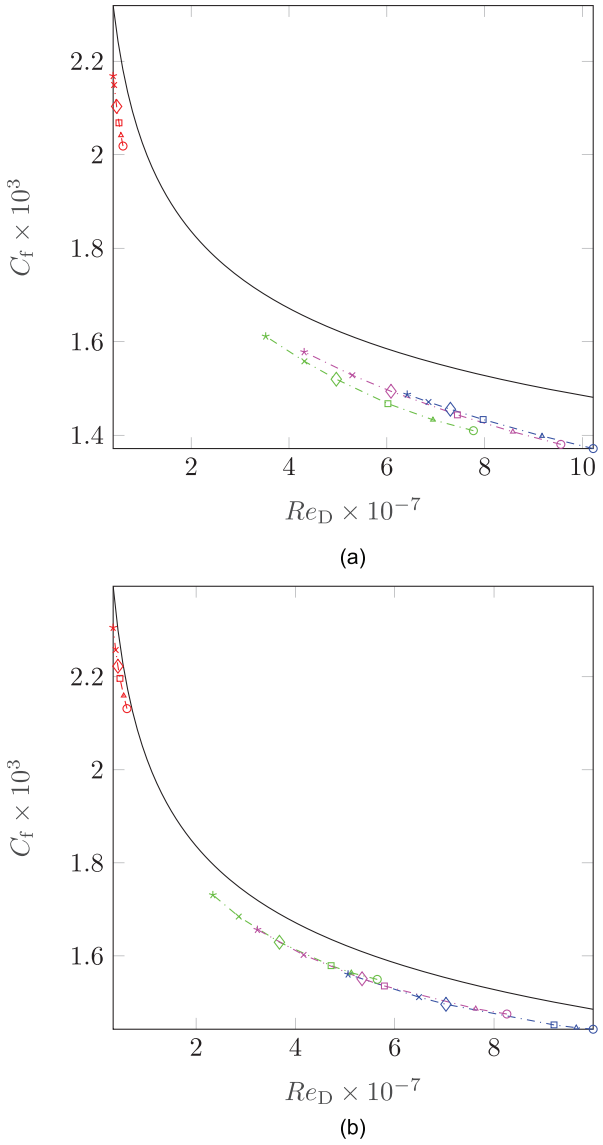

FIG. 10. Friction coefficient C_f vs Reynolds number Re_D for compressible pipe flows. (a) air (ideal gas) and (b) siloxane MM. The values of C_f obtained from CFD simulations are compared with the values calculated with the empirical Colebrook–White correlation. Blue dotted line: case Z05; green dotted line: case Z07sub; pink dotted line: case Z07super; red dotted line: case Z1; black continuous line: Colebrook–White correlation.

The viscous equations governing adiabatic flows that can be obtained in terms of the coefficients listed in Table II were solved to evaluate the influence of both the fluid molecular complexity and dense vapor effects. The hydraulic diameter of the pipe is constant and equal to 0.1 m.

Figures 11(a) and 11(b) show the Fanno curves evaluated for $Z \simeq 0.5$ and $Z \simeq 1$. The entropy production is plotted in terms of the local entropy loss coefficient $T\Delta s/u_{in}^2$. The results are displayed for the

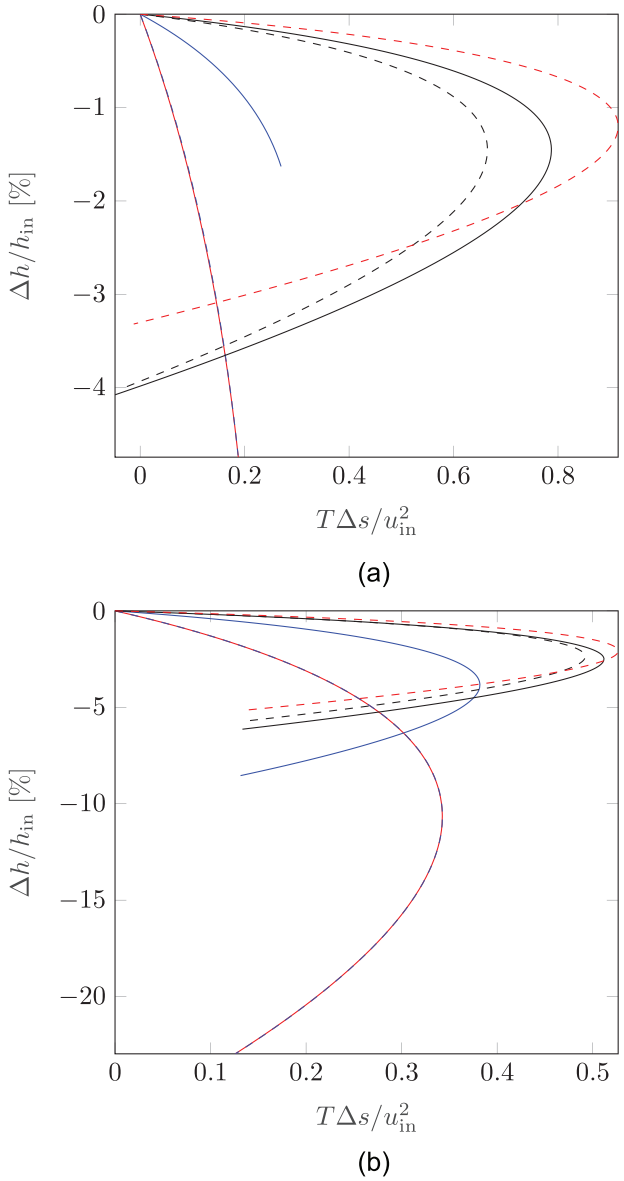

FIG. 11. Fanno curves in the non-dimensionalized $h - s$ thermodynamic plane for different fluids at fixed inlet Mach number, $M_{\rm in} = 0.7$. The considered fluids can be identified with the colors and markers reported in Table IV. Two sets of inlet reduced temperatures and pressures are reported: (a) $T_{\rm r} = 1.05$, $p_{\rm r} = 1.15$; and (b) $T_{\rm r} = 0.9$, $p_{\rm r} = 0.05$.

fluids of Table IV. The inlet Mach number is set to $M_{\rm in} = 0.7$. The molecular complexity of the fluid affects the value of Δh required to choke the flow for both the $Z \simeq 0.5$ and $Z \simeq 1$ cases. The combination of the enthalpy and entropy equations, see Table II, yields

$$\frac{1}{T}\frac{{\rm d}h}{{\rm d}s} = -(G+1)\frac{M^2}{1-M^2}. \tag{28}$$

This relation shows that the slope of the Fanno curve depends on the value of G. As a consequence, the enthalpy drop that causes the flow to be choked decreases with increasing fluid molecular complexity and normalized entropy generation. If the fluid states are in proximity of the critical point at the inlet (case $Z \simeq 0.5$), the enthalpy drop at choking conditions is lower than the enthalpy drop leading to choking in case the fluid is in the dilute gas state. This finding is valid for all the investigated fluids and is related to the larger value of the dense-vapor isobaric heat capacity if compared to the ideal gas value.

Figures 12(a) and 12(b) show that the pipe length L^* required for the flow to be choked is significantly longer for flows of fluids made of complex molecules, regardless of the thermodynamic state and the inlet Mach number. This is a consequence of the higher entropy generation in choked Fanno flows of low-G fluids, see Fig. 11: viscous dissipation at the walls induces viscous heating of the flow; thus, complex molecules of organic dense vapors allow a larger amount of the energy to be stored as internal energy of the fluid with negligible or minor increase in the fluid temperature. Moreover, a smaller amount of internal energy is converted into kinetic energy; from Table II, it follows that

$$\frac{{\rm d}E_{\rm k}}{E_{\rm k}} = (G+1)\frac{M^2}{1-M^2}\frac{4C_{\rm f}{\rm d}x}{d_{\rm H}}. \tag{29}$$

This equation shows that, if different fluids are compared at fixed reduced temperature and pressure at the inlet, the variation of kinetic energy of the fluid is affected more by the decrease in the value of G than by the increase in the value of $C_{\rm f}$, see Figs. 12(c) and 12(d). Therefore, the increase in kinetic energy is low in flows of fluids made of complex molecules. As a consequence, in these flows, the fluid acceleration is smaller and choking occurs further downstream. Furthermore, L^* increases if the fluid state approaches the critical point of the substance, regardless of its molecular complexity, due to the large value of the heat capacity in the dense vapor thermodynamic region, see Eq. (22).

Figures 13(a) and 13(b) show the variation of Mach number with the normalized pipe axial coordinate at different inlet Mach numbers. The results are reported for nitrogen [Fig. 13(a)] and siloxane D_6 [Fig. 13(b)]. The same sets of inlet reduced temperature, reduced pressure, and Mach number introduced in Sec. IV A are also used here to fix the conditions of the flow. If the fluid is in the dilute gas state, the Mach number increases monotonically with the axial coordinate. At fixed normalized axial coordinate, the Mach number increases less in the case of flows of fluids made of complex molecules, such as siloxane D_6. However, if the fluid is in a thermodynamic state close to that of the critical point, the trend of the Mach number as a function of the axial coordinate becomes non-monotone for Fanno flows of D_6: after an initial decrease, it reaches a minimum and then increases. Solving ${\rm d}M/M = f(4C_{\rm f}{\rm d}x/d_{\rm H}) = 0$ yields an analytical relation for the minimum value of the Mach number, namely,

$$M_{\rm min} = \sqrt{1 - \frac{2\Gamma}{\Psi}\frac{G+1}{G}}, \tag{30}$$

which is defined for

$$\Gamma \geq \frac{\Psi}{2}\frac{G}{G+1}. \tag{31}$$

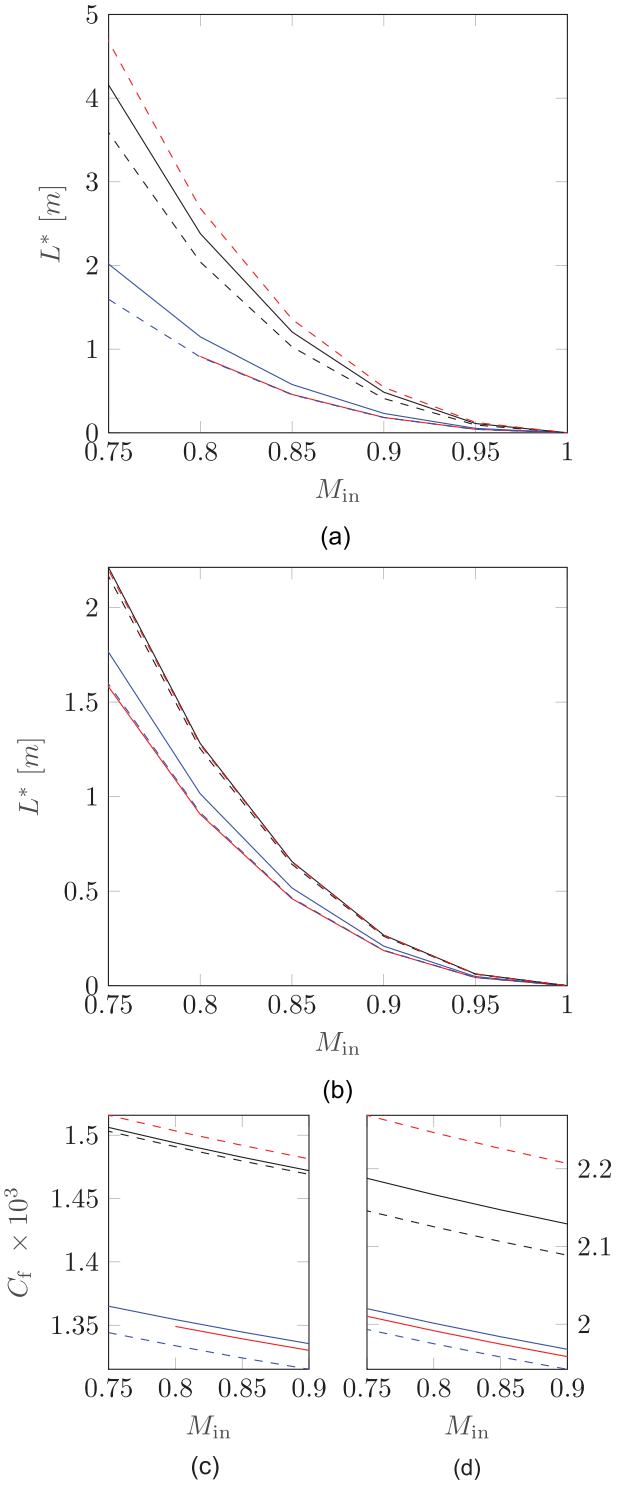

FIG. 12. Pipe length required to choke the flow vs inlet Mach number. Two sets of inlet reduced temperature and pressure are considered: (a) $T_r = 1.05$, $p_r = 1.15$; (b) $T_r = 0.9$, $p_r = 0.05$. (c) and (d) depicts the variation of the friction coefficient with the inlet Mach number corresponding to the cases of figures (a) and (b), respectively. Fluids are labeled with the colors and the markers reported in Table IV.

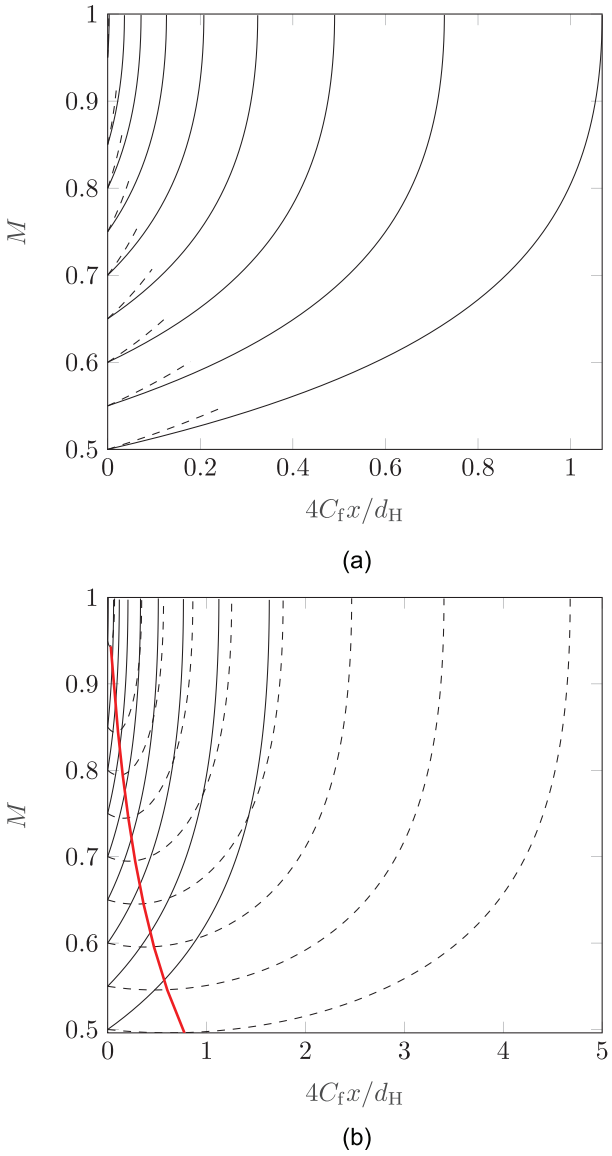

FIG. 13. Mach number vs non-dimensional axial pipe coordinate for Fanno flows of (a) nitrogen and (b) siloxane D_6 for different inlet Mach numbers. Two sets of inlet reduced temperature and pressures are considered: ····· $T_r = 1.05$, $p_r = 1.15$; and — $T_r = 0.9$, $p_r = 0.05$.

If the fluid is in the dilute gas state, $Z \to 1$, $2\Gamma/\Psi(G+1)/G \to (\gamma+1)/(\gamma-1)$, and M_{min} does not admit real solutions. The red line in Fig. 13(b) identifies the locus of M_{min} for different values of the inlet Mach number. Figure 9 shows the thermodynamic region formed by states for which (31) holds in the temperature-entropy diagram of D_6. Calculations based on state-of-the-art thermophysical models highlighted that fluids with $G_\infty < 0.0128$ admit a thermodynamic region where relation (31) is satisfied. The term $G/(G+1)$ is always greater than one. As a consequence, compared to Rayleigh flows, only a few fluids, mainly BZT fluids, exhibit a thermodynamic region where Eq. (30) admits a real solution.

V. MIXING OF DENSE VAPORS STREAMS

Two configurations of mixing flows are considered, namely, the co-flowing of two streams in either thermal or kinematic non-equilibrium and the injection of a flow into a main stream. Co-flowing mixing is representative, for example, of flow phenomena occurring in turbomachines and heat exchangers, like wake mixing downstream of a blade or a blunt body, while flow injection resembles, for example, tip leakage flow. For the case of co-flowing mixing, entropy generation is calculated by applying the conservation laws and models for thermodynamic and transport properties of the fluid to the control volume sketched in Fig. 4(b) and assuming a mixed-out state at the outlet. The wall shear and the heat flux from the wall are neglected. The irreversible entropy generation is expressed in terms of loss coefficient as

$$\zeta_{s,\mathrm{irr}} = \frac{\bar{T}_{\mathrm{in,t}}(s_{\mathrm{out}} - s_{\mathrm{in}})}{\frac{1}{2}\bar{u}_{\mathrm{in}}^2}, \tag{32}$$

where $\bar{T}_{\mathrm{in,t}}$ is the stagnation inlet temperature averaged over the mass flow, $\bar{u}_{\mathrm{in}}$ is the mass-flow-averaged velocity at the inlet, and s_{out} is the mixed-out entropy at the outlet boundary. Two sets of inlet thermodynamic conditions are considered, namely, $\bar{T}_{\mathrm{r,in}} = 0.85$, $\bar{p}_{\mathrm{r,in}} = 0.01$ and $\bar{T}_{\mathrm{r,in}} = 1.05$, $\bar{p}_{\mathrm{r,in}} = 1.15$, where $\bar{T}_{\mathrm{r,in}}$ and $\bar{p}_{\mathrm{r,in}}$ denote the mass-flow-averaged static temperature and pressure at the inlet. The first set of conditions is representative of a dilute gas case ($Z \simeq 1$), while the second of a flow is occurring with the fluid states in proximity of the vapor–liquid critical point of the fluid ($Z \simeq 0.5$).

To study the effect of kinematic non-equilibrium, the reduced temperature of both streams is set to $\bar{T}_{\mathrm{r,in}}$, while M_1 and M_2 are both set to $\bar{M}_{\mathrm{in}} \pm \Delta M/2$, where $\bar{M}_{\mathrm{in}} = 0.6$. Similarly, the effect of thermal non-equilibrium is evaluated by imposing $M_1 = M_2 = \bar{M}_{\mathrm{in}}$ and T_1 and T_2 both equal to $\bar{T}_{\mathrm{r,in}} \pm \Delta T_{\mathrm{r}}/2$.

Figure 14(a) shows the results of the calculation of the entropy loss coefficient for flows in kinematic non-equilibrium and for the two considered sets of inlet conditions. It can be observed that the trend of the loss coefficient is barely dependent on both molecular complexity and dense vapor effects. Furthermore, the entropy generation solely depends on ΔM: the higher ΔM between the two streams, the higher the resulting $\zeta_{s,\mathrm{irr}}$. Conversely, the fluid non-ideality and its molecular complexity affect the entropy loss in the case of thermal non-equilibrium. If the inlet conditions are close to the critical point [Fig. 14(b)], the irreversible entropy loss coefficient increases regardless of the fluid. According to Greitzer *et al.*,[55] Chap. 1, the entropy production in a process in which heat transfer across a finite temperature difference occurs is proportional to the thermal conductivity of the fluid. Figures 14(c) and 14(d) illustrate the trends of the thermal conductivity of the fluid evaluated in the $Z \simeq 0.5$ and $Z \simeq 1$ cases, respectively. On a qualitative basis, it can be inferred that the thermal conductivity of the fluid increases as the state of the fluid departs from the dilute gas state. Furthermore, molecular complexity has a significant impact on the value of ζ_s. This trend is in accordance with what can be deduced from the equations governing the case of flow injection into a main stream [Eq. (34)], which refer to a different flow configuration but the flow is subjected to same underlying physics. A strictly physical explanation of the trend could not be fully clarified. However, the larger the specific heat capacity of the fluid, the lower is the related temperature change for a fixed amount of exchanged thermal energy between the different streams. Therefore, low G fluids in proximity of

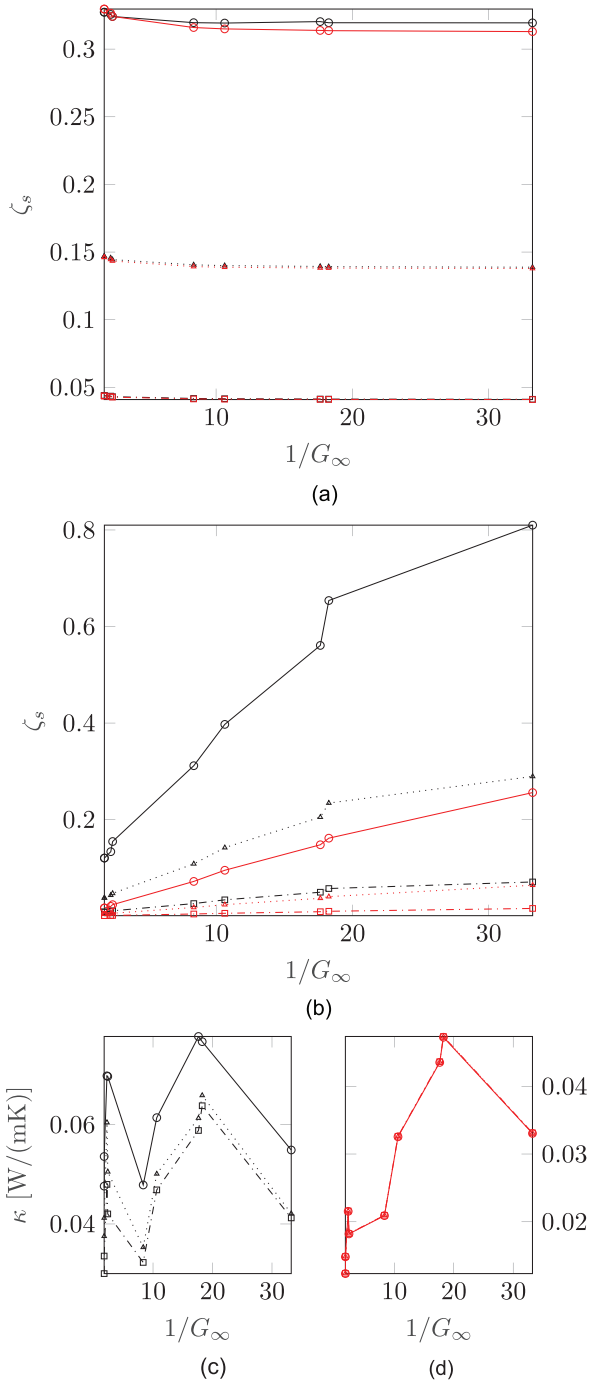

FIG. 14. Irreversible entropy loss coefficient vs molecular complexity for mixing streams in (a) kinematic or (b) thermal non-equilibrium. Inlet thermodynamic conditions: $\bar{T}_{\mathrm{r,in}} = 0.85$, $\bar{p}_{\mathrm{r,in}} = 0.01$, $Z \simeq 1$ (red) and $\bar{T}_{\mathrm{r,in}} = 1.05$, $\bar{p}_{\mathrm{r,in}} = 1.15$ $Z \simeq 0.5$ (black). In figure (a), - - - □ - - -: $\Delta M = 0.2$, ····Δ····: $\Delta M = 0.6$, —○—: $\Delta M = 1$. In figure (b), - - - □ - - -: $\Delta T/T_{\mathrm{crit}} = 2\%$, ····Δ····: $\Delta T/T_{\mathrm{crit}} = 6\%$, —○—: $\Delta T/T_{\mathrm{crit}} = 10\%$. For the case of thermal non-equilibrium, values of thermal conductivity vs molecular complexity evaluated for each fluid at $Z \simeq 0.5$ (c) and $Z \simeq 1$ (d) are reported. The same legend of figure (b) applies to both charts.

the critical point tend to remain in thermal non-equilibrium, thus increasing the irreversible entropy generation.

Contrary to the case of co-flow mixing, the entropy loss coefficient for the flow injection configuration is an analytical expression if the mass flow rate of the injected flow is small compared to that of the main stream. The control volume for the analysis of this mixing configuration is shown in Fig. 4(a); here, the contributions due to changes in cross-sectional area, wall friction, energy transfer as heat and shaft work are neglected. The fluid of the two streams is the same and the two streams are in mechanical equilibrium with each other, i.e., the mixing occurs at fixed pressure value. This implies that the specific enthalpy of the injected flow after the mixing process is the same of that of the main flow, i.e., $h_{\text{inj}} = h$.

The conservation equations in differential form are reported in Sec. III, namely, Eqs. (16)–(18). The wall viscous effects term is neglected, while the terms related to energy transfer as heat to the flow, to shaft work and to variations in the cross-sectional area do not apply. Hence, following the same approach reported in Sec. III and Appendix B, one can obtain a relation for the entropy variation of the main stream, namely,

$$\frac{\mathrm{d}s}{c_p} = \frac{\mathrm{d}\dot{m}}{\dot{m}}\left\{\frac{h_{\text{inj}}(T_{\text{inj}}) - h_{\text{inj}}(T)}{c_p T} + \frac{1}{2}\frac{G^2M^2}{\gamma - 1} \times \left[\left(\frac{u_{\text{inj}}}{u}\right)^2 + -2\left(\frac{u_{\text{inj}}}{u}\right)\cos\alpha + 1\right]\right\}. \tag{33}$$

The irreversible entropy loss due to mixing is $\mathrm{d}s_{\text{irr}} = \mathrm{d}s - (s_{\text{inj}} - s)\mathrm{d}\dot{m}/\dot{m}$, where s and s_{inj} are the inlet entropy of the main and the injected streams, respectively.[70] By multiplying this relation by $2T/u^2$ and combining it with Eq. (A13), the entropy loss coefficient can be expressed as

$$\zeta_{s,\text{irr}} = \zeta_s - \frac{2(\gamma - 1)}{G^2M^2}\frac{(s_{\text{inj}} - s)}{c_p}\frac{\mathrm{d}\dot{m}}{\dot{m}}, \tag{34}$$

where

$$\zeta_s = \frac{T\mathrm{d}s}{u^2/2} = \frac{\mathrm{d}\dot{m}}{\dot{m}}\left\{\frac{2(\gamma - 1)}{G^2M^2}\frac{h_{\text{inj}}(T_{\text{inj}}) - h_{\text{inj}}(T)}{c_p T} + \left[\left(\frac{u_{\text{inj}}}{u}\right)^2 - 2\left(\frac{u_{\text{inj}}}{u}\right)\cos\alpha + 1\right]\right\}. \tag{35}$$

Equation (34) points out the contributions of kinematic and of thermal non-equilibrium to the irreversible entropy generation. The second term of Eq. (35) depends solely on the velocity difference between the two streams and on the injection angle, hence, in the case of thermal equilibrium of the two streams, entropy generation is not affected by the state of the fluid and its molecular complexity. The charts in Fig. 14 related to the mixing of co-flowing streams show that in both configurations, molecular complexity and thermodynamic fluid state do not play a role. Conversely, in the case of thermal non-equilibrium, they affect irreversible entropy generation.

More insights could be obtained by numerically solving Eq. (34) for two sets of inlet thermodynamic conditions, namely, $T_r = 1.05$, $p_r = 1.15$ (ideal gas) and $T_r = 1.05$, $p_r = 0.01$ (dense vapor, $Z \simeq 0.5$). For both cases, three different inlet Mach numbers, namely, $M = 0.3$, $M = 0.8$, and $M = 1.2$, and two sets of the injected flow temperature ratios were considered, i.e., $T_{\text{inj}}/T = 0.95$ and $T_{\text{inj}}/T = 1.05$. For all cases, the ratio between the injected and main stream mass flows $\mathrm{d}\dot{m}/\dot{m}$ was set to 0.01. Figures 15(a) and 15(b) display the results for the cases $Z \simeq 0.5$ and $Z \simeq 1$, respectively. If the inlet thermodynamic conditions depart significantly from those of the critical point, the dissipation linearly increases with molecular complexity. As $Z \to 1$, Eq. (34) resembles the ideal gas formulation reported in Greitzer *et al.*[55] As a consequence, $\zeta_{s,\text{irr}}$ only depends on the ratio T_{inj}/T and on G_∞, given that $(\gamma - 1) \to G_\infty$. For fixed values of T_{inj}/T and M, $\zeta_{s,\text{irr}}$ decreases with G_∞. From Eqs. (34) and (35), it can

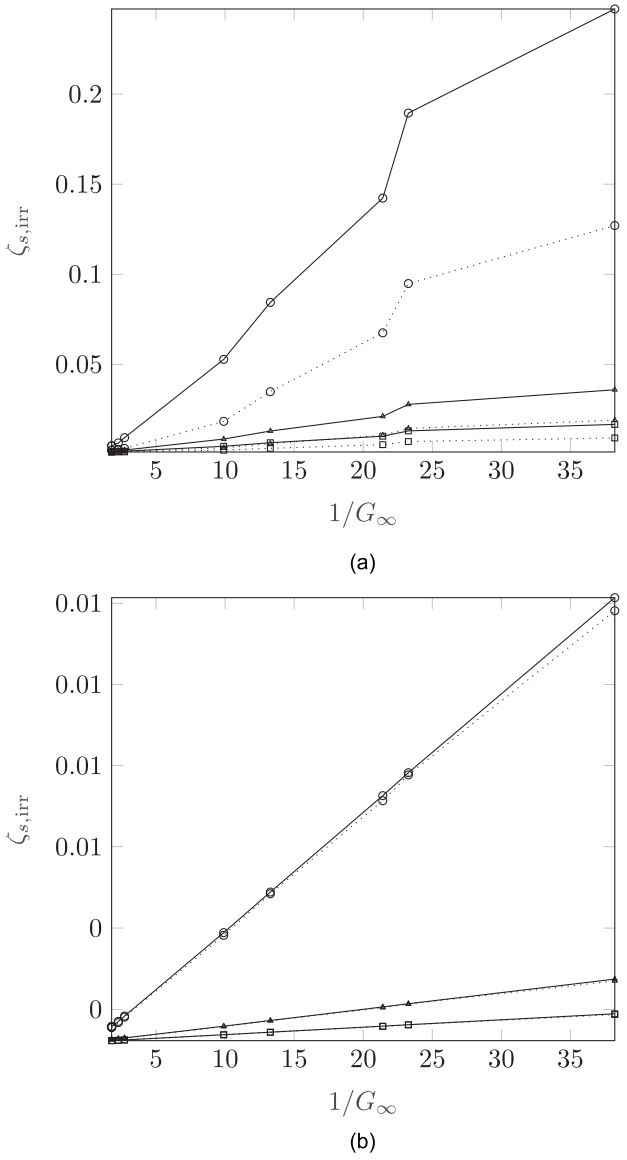

FIG. 15. Irreversible entropy loss coefficient vs molecular complexity in flows with fluid states featuring (a) $Z \simeq 0.5$ and (b) $Z \simeq 1$. For both figures, ——: $T_{\text{inj}}/T = 0.95$, · · · · · ·: $T_{\text{inj}}/T = 1.05$, ○: $M = 0.3$, △: $M = 0.8$, and □: $M = 12$.

be also inferred that the injection of a cooler stream leads to a higher entropy generation. Furthermore, the dissipation decreases with the Mach number of the main flow.

The same observations apply to the $Z \simeq 0.5$ case. However, $\zeta_{s,\mathrm{irr}}$ increases of up to one order of magnitude for flows of complex molecules in thermodynamic states in the vicinity of the vapor–liquid critical point state [Fig. 15(a)]. In accordance with Eq. (34), the charts show that reversible entropy generation increases in case the injected flow is cooler. In addition, as $\gamma \to \infty$, for thermodynamic states in proximity of that of the critical point, regardless of the fluid, the effect of γ prevails on the effect of G.

VI. CONCLUSION

This study is related to the investigation of the impact of fluid molecular complexity and dense vapor effects on paradigmatic one-dimensional flows, namely, Rayleigh and Fanno flows, together with the mixing of two streams in kinematic and thermal non-equilibrium. The theoretical framework for the analysis of one-dimensional flows of perfect gases has been extended to the case of non-ideal compressible flows. Flows of several fluids at different reduced thermodynamic inlet conditions have been considered. State-of-the-art thermophysical models have been used to accurately estimate the thermodynamic and transport properties of the fluids.

Based on the results of the numerical analysis, the following conclusive remarks can be drawn.

(1) The molecular complexity of a fluid scales with the inverse of the Grüneisen parameter G for a given thermodynamic state. In particular, the Grüneisen parameter evaluated for $v \to \infty$ is inversely proportional to the number of molecular degrees of freedom of the fluid molecule. This relation is qualitatively valid also for fluid states close to the vapor–liquid critical point. The Grüneisen parameter G is, therefore, arguably the best parameter to characterize molecular complexity given that it appears explicitly in paradigmatic flow equations.
(2) In Rayleigh flows, the ratio between kinetic and internal energy of the fluid is determined by the complexity of the fluid molecules, as expected. The Grüneisen parameter determines the value of this ratio and affects the amount of energy transfer as heat causing flow choking.
(3) RANS CFD simulations of subsonic channel flows showed that the Fanning friction coefficient C_f is arguably independent of the flow Mach number, if the fluid is made of complex molecules. As a consequence, the Colebrook–White empirical correlation valid for incompressible flows provides accurate values of C_f as a function of the Reynolds number Re_D even if the flow is compressible.
(4) In a Fanno flow, the molecular complexity of the fluid determines the location at which the flow is choked, which increases with increasing molecular complexity.
(5) The relation between the Mach number and the production of entropy in Rayleigh and Fanno flows of complex-molecule fluids is non-monotonic if the inlet fluid state is at conditions close to those of the vapor–liquid critical point. The minimum value of the Mach number is dependent on the fluid thermodynamic variables Γ, Ψ, and G.
(6) In flows in which two streams at different inlet velocity and temperature mix, thermal non-equilibrium between the streams induces a larger dissipation in fluids characterized by high complexity of the molecular structure. Furthermore, the dissipation increases if the fluid state at the inlet of the channels approaches the vapor–liquid critical state.
(7) The value of the Eckert number decreases with the complexity of the fluid molecular structure. As a consequence, thermal and dynamic effects can be decoupled, to a large extent, in fluids characterized by a high molecular complexity.

Future research will aim at validating the obtained trends with high-fidelity numerical simulations and experiments in boundary layers and mixing processes in dense vapor flows. Additional research will also involve the estimation of the influence of both two-phase flows and mixtures of fluids on the one-dimensional processes considered here.

ACKNOWLEDGMENTS

This research has been supported by the Applied and Engineering Sciences Domain (TTW) of the Dutch Organization for Scientific Research (NWO), Technology Program of the Ministry of Economic Affairs, Grant No. 15837.

APPENDIX A: USEFUL RELATIONS BETWEEN FLUID PARAMETERS

The derivation of analytical relations between some of the non-dimensional fluid parameters introduced in Sec. II is reported here for convenience. In a dense vapor, the specific enthalpy depends on both temperature and pressure, i.e., $h = h(T, p)$. The differential of the specific enthalpy reads

$$\mathrm{d}h = \left(\frac{\partial h}{\partial T}\right)_p \mathrm{d}T + \left(\frac{\partial h}{\partial p}\right)_T \mathrm{d}p = c_p \mathrm{d}T + \left(\frac{\partial h}{\partial p}\right)_T \mathrm{d}p. \tag{A1}$$

Differentiating the Gibbs equation $\mathrm{d}h = T\mathrm{d}s + v\mathrm{d}p$ with respect to pressure at constant density yields

$$\left(\frac{\partial h}{\partial p}\right)_T = v + T\left(\frac{\partial s}{\partial p}\right)_T. \tag{A2}$$

Using the Maxwell relation $(\partial s/\partial p)_T = (\partial v/\partial T)_p$[71] and substituting Eq. (A2) into Eq. (A1) gives

$$\begin{aligned}\mathrm{d}h &= c_p \mathrm{d}T + \left[v - T\left(\frac{\partial v}{\partial T}\right)_p\right]\mathrm{d}p \\ &= c_p \mathrm{d}T + \frac{(1-\beta_p T)}{\rho}\mathrm{d}p,\end{aligned} \tag{A3}$$

where β_p is the isobaric compressibility, as reported in Table I. Equation (A3) can be substituted into the Gibbs equation to obtain

$$\mathrm{d}s = c_p \frac{\mathrm{d}T}{T} - \beta_p \frac{p}{\rho}\frac{\mathrm{d}p}{p}. \tag{A4}$$

The total differential of the entropy $s = s(p, T)$ is given by

$$\mathrm{d}s = \left(\frac{\partial s}{\partial T}\right)_p \mathrm{d}T + \left(\frac{\partial s}{\partial p}\right)_T \mathrm{d}p. \tag{A5}$$

Combining this equation with Eq. (A4) gives

$$\frac{c_p}{T}=\left(\frac{\partial s}{\partial T}\right)_p=\left(\frac{\partial p}{\partial T}\right)_s\left(\frac{\partial v}{\partial T}\right)_p=\left(\frac{\partial p}{\partial T}\right)_s\frac{\beta_p}{\rho}, \tag{A6}$$

which is obtained with the help of the so-called chain rule and the Maxwell relation $(\partial s/\partial p)_T=(\partial v/\partial T)_p$.

Similarly, by using the relations $e=e(T,v)$, $s=s(T,v)$, the Gibbs equation and the relations between thermodynamic derivatives listed in Bridgman,[71] one can also obtain

$$\frac{c_v}{T}=\left(\frac{\partial s}{\partial T}\right)_v=-\left(\frac{\partial p}{\partial T}\right)_v\left(\frac{\partial v}{\partial T}\right)_s. \tag{A7}$$

Here, again the chain rule and the Maxwell relation $(\partial s/\partial p)_v=-(\partial v/\partial T)_s$ have been used. A simple algebraic manipulation of Eqs. (A6) and (A7) leads to

$$\frac{c_p-c_v}{c_v}=\frac{\gamma-1}{\gamma}=\left(\frac{\partial p}{\partial T}\right)_v\left(\frac{\partial T}{\partial p}\right)_s=\frac{\beta_p}{\beta_T}\left(\frac{\partial T}{\partial p}\right)_s. \tag{A8}$$

Differentiating the equation $Tp^{-\gamma_{pT}}=\text{const.}$ gives

$$\left(\frac{\partial T}{\partial p}\right)_s=\gamma_{pT}\frac{T}{p}. \tag{A9}$$

The combination of Eqs. (A6) and (A9) provides

$$\gamma_{pT}=\frac{\beta_p}{c_p}\frac{p}{\rho}, \tag{A10}$$

similarly, Eq. (A8) can be combined with Eq. (A9) to obtain

$$\gamma_{pT}=\frac{\gamma-1}{\gamma}\frac{\beta_T p}{\beta_p T}. \tag{A11}$$

By manipulating Eqs. (5), (11), (A10), and (A9), a relation between γ_{pv}, G, β_p, and β_T can be found and is

$$\frac{\beta_p}{c_p}\frac{p}{\rho}=\frac{\gamma-1}{\gamma}\frac{\beta_T p}{\beta_p T}=\frac{G}{\gamma_{pv}}. \tag{A12}$$

The sound speed in a dense vapor can be expressed in terms of γ_{pv} and G using Eqs. (5), (11), and (A12) as

$$c^2=\left(\frac{\partial p}{\partial \rho}\right)_s=\gamma_{pv}\frac{p}{\rho}=\frac{G^2}{\gamma-1}c_pT. \tag{A13}$$

Finally, the combination of (A13) with (A12) allows us to write

$$\frac{p}{\rho u^2}=\frac{1}{\gamma_{pv}M^2}. \tag{A14}$$

APPENDIX B: DERIVATION OF THE INFLUENCE COEFFICIENTS

The general volumetric equation of state valid for dense vapors $p=\rho ZRT$ is adopted to derive some relations among the fluid properties that are used to obtain expressions for the influence coefficients. Differentiation of the volumetric equation of state gives

$$\frac{\mathrm{d}p}{p}=\frac{\mathrm{d}\rho}{\rho}+\frac{\mathrm{d}T}{T}+\frac{\mathrm{d}Z}{Z}. \tag{B1}$$

Given that $Z=Z(p,T)$, the first-order expansion of the differential dZ yields

$$\frac{\mathrm{d}Z}{Z}=\frac{T}{Z}\left(\frac{\partial Z}{\partial T}\right)_p\frac{\mathrm{d}T}{T}+\frac{p}{Z}\left(\frac{\partial Z}{\partial p}\right)_T\frac{\mathrm{d}p}{p}. \tag{B2}$$

Using the relations reported in Table I, this expression can be substituted into Eq. (B1) to obtain

$$\beta_T p\frac{\mathrm{d}p}{p}-\beta_p T\frac{\mathrm{d}T}{T}=\frac{\mathrm{d}\rho}{\rho}, \tag{B3}$$

or, alternatively, making use of the definitions of γ_{pv} and G, one obtains

$$\frac{\gamma}{\gamma_{pv}}\frac{\mathrm{d}p}{p}-\frac{\gamma-1}{G}\frac{\mathrm{d}T}{T}=\frac{\mathrm{d}\rho}{\rho}. \tag{B4}$$

The combination of Eq. (A3) reported in Appendix A with Eqs. (A12) and (11) gives

$$\frac{\mathrm{d}h}{c_pT}=\frac{\mathrm{d}T}{T}+\frac{G-(\gamma-1)}{\gamma_{pv}}\frac{G}{\gamma-1}\frac{\mathrm{d}p}{p}. \tag{B5}$$

Manipulating the Gibbs equation, together with Eqs. (B5) and (A12), provides a relation for the specific entropy variation, i.e.,

$$\frac{\mathrm{d}s}{c_p}=\frac{\mathrm{d}T}{T}-\frac{G}{\gamma_{pv}}\frac{\mathrm{d}p}{p}. \tag{B6}$$

Consider now the momentum equation (17). The friction term can be rewritten as a function of the non-dimensional friction coefficient C_f and of the so-called hydraulic diameter, defined as $d_H=4A/p_w$, where p_w is the wet perimeter. Dividing all the terms of the equation by $\rho u^2 A$ yields

$$\frac{\mathrm{d}u}{u}+\frac{p}{\rho u^2}\frac{\mathrm{d}p}{p}=-\frac{-\mathrm{d}w_{shaft}}{u^2}-\frac{1}{2}4C_f\frac{\mathrm{d}x}{d_H}+\frac{\mathrm{d}\dot{m}}{\dot{m}}\left(\frac{u_{inj}}{u}\cos\alpha-1\right). \tag{B7}$$

Equations (A13) and (A14) can be substituted into the momentum equation (B7) to obtain

$$\frac{\mathrm{d}u}{u}+\frac{1}{\gamma_{pv}M^2}\frac{\mathrm{d}p}{p}=-\frac{(\gamma-1)}{G^2M^2}\frac{-\mathrm{d}w_{shaft}}{c_pT}-\frac{1}{2}4C_f\frac{\mathrm{d}x}{d_H}+\frac{\mathrm{d}\dot{m}}{\dot{m}}\left(\frac{u_{inj}}{u}\cos\alpha-1\right), \tag{B8}$$

where the Mach number is used in place of the speed of sound. The energy equation (18) can be manipulated to find a relation between pressure and temperature. Dividing all terms by c_{pT} and inserting Eqs. (A13), (A14), and (B5) yields

$$\frac{\mathrm{d}T}{T}+\frac{G-(\gamma-1)}{\gamma_{pv}}\frac{G}{\gamma-1}\frac{\mathrm{d}p}{p}+\frac{G^2M^2}{\gamma-1}\frac{\mathrm{d}u}{u}=\frac{-\mathrm{d}q}{c_pT}-\frac{-\mathrm{d}w_{shaft}}{c_pT}+\left\{\frac{h_{inj,in}-h_{inj}}{c_pT}+\frac{1}{2}\frac{G^2M^2}{\gamma-1}\left[\left(\frac{u_{inj}}{u}\right)^2-1\right]\right\}\frac{\mathrm{d}\dot{m}}{\dot{m}}. \tag{B9}$$

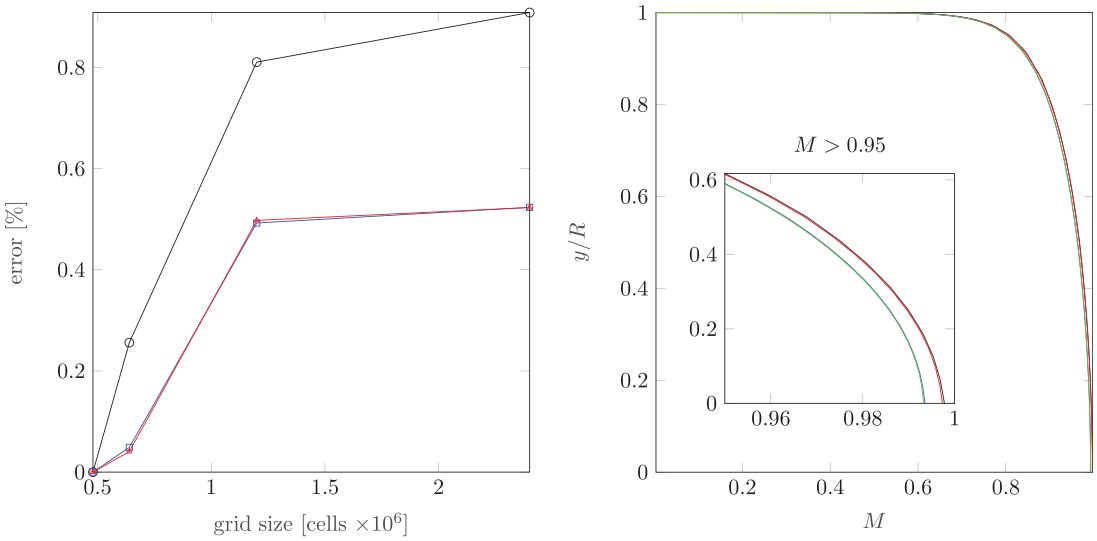

FIG. 16. Grid independence study. (a) Relative deviation, as a function of the computational mesh size, of the values of —○— C_f, —□— M, and —△— Re_D from the ones computed using the coarsest mesh of 480 000 cells. Each variable is calculated with a mass flow average over the outlet section of the pipe. (b) Mach number at the outlet pipe section vs normalized radial coordinate for four different computational grids. Grid size: black line: 480 000, red line: 640 000 blue line 1.2M, green line: 24M. A close-up of the Mach profile in proximity of the pipe centerline is also displayed.

Consider $c = c(\rho, s)$; the total differential of the speed of sound can, therefore, be written as

$$\mathrm{d}c = \left(\frac{\partial c}{\partial \rho}\right)_s \mathrm{d}\rho + \left(\frac{\partial c}{\partial s}\right)_\rho \mathrm{d}\rho. \tag{B10}$$

Using the definition of the fundamental derivative of gas dynamics [Eq. (1)], the first derivative in Eq. (B10) can be rewritten as

$$\left(\frac{\partial c}{\partial \rho}\right)_s = (\Gamma - 1)\frac{c}{\rho}. \tag{B11}$$

The Maxwell thermodynamic relations and Eq. (10) can be combined to obtain a formulation for the derivative appearing as the second term of Eq. (B10), i.e.,

$$\begin{aligned}\left(\frac{\partial c}{\partial s}\right)_\rho &= \frac{1}{2c}\left(\frac{\partial c^2}{\partial s}\right)_\rho = \frac{1}{2c}\frac{(\partial c^2/\partial p)_\rho (\partial p/\partial T)_\rho}{(\partial s/\partial e)_\rho (\partial e/\partial T)_\rho} \\ &= G\frac{T}{2c}\Psi = \frac{\gamma - 1}{\beta_p T}\frac{T}{2c}\Psi,\end{aligned} \tag{B12}$$

where $(\partial s/\partial e)_\rho = 1/T$ according to Bridgman[71] and $(\partial e/\partial T)_\rho = c_v$. The combination of the last two relations with Eq. (B10) yields

$$\begin{aligned}\frac{\mathrm{d}c}{c} &= (\Gamma - 1)\frac{\mathrm{d}\rho}{\rho} + \frac{\gamma - 1}{\beta_p T}\frac{T}{2c}\Psi = (\Gamma - 1)\frac{\mathrm{d}\rho}{\rho} + \beta_p T\frac{\Psi}{2}\frac{\mathrm{d}s}{c_p} \\ &= (\Gamma - 1)\frac{\mathrm{d}\rho}{\rho} + \frac{\gamma - 1}{G}\frac{\Psi}{2}\frac{\mathrm{d}s}{c_p}.\end{aligned} \tag{B13}$$

Note that the second term cancels out if the process is isentropic. Given that $M \equiv u/c$, it is also possible to relate the change of speed of sound to the change of Mach number via

$$\frac{\mathrm{d}M}{M} = \frac{\mathrm{d}u}{u} - \frac{\mathrm{d}c}{c}. \tag{B14}$$

The combination of Eqs. (16), (B4)–(B6), (B8), (B9), (B13), and (B14) provides analytical relations between each flow quantity and changes of cross-sectional area, energy transfer as heat, shaft work, wall friction, and mass flow injection. These relations are summarized in Table II and can be formally expressed through the synthetic formulation reported in Eq. (19). Neglecting the contributions due to shaft work, energy transfer as heat, wall friction, and changes of cross section, the entropy increase in the main flow due to fluid injection in the control volume can also be retrieved. In particular, the combination of Eqs. (16), (B6), (B8), and (B9) results in Eq. (33).

APPENDIX C: MESH SENSITIVITY ANALYSIS

A study of the sensitivity to the grid resolution for the CFD simulations treated in Sec. IV B was performed. Simulations of flows of siloxane MM with $T_{r,out} = 1.05$, $p_{r,out} = 1.15$ at the pipe outlet and $p_{t,r} = 1.7$ at the inlet were run for several grids with different levels of refinement. A total of four grids with 480 000, 640 000, 1.2 $\times$ 10^6, and 2.4 $\times$ 10^6 cells were considered. Figure 16 shows the results of the mesh sensitivity analysis. The relative deviation of the values of C_f, M, and Re_D between the finest and the coarsest grid is <1% for all variables, see Fig. 16(a). Minimal differences depending on the grid density were also observed in terms of Mach number profile at the pipe outlet [Fig. 16(b)]: the largest difference is of 0.4% at the channel mid-line.

DATA AVAILABILITY

The data that support the findings of this study are available from the corresponding author upon reasonable request.

REFERENCES

[1]H. Nemati, A. Patel, B. J. Boersma, and R. Pecnik, "Mean statistics of a heated turbulent pipe flow at supercritical pressure," Int. J. Heat Mass Transfer **83**, 741–752 (2015).

[2]P. Colonna, E. Casati, C. Trapp, T. Mathijssen, J. Larjola, T. Turunen-Saaresti, and A. Uusitalo, "Organic Rankine cycle power systems: From the concept to current technology, applications, and an outlook to the future," J. Eng. Gas Turbines Power **137**, 100801 (2015).

[3]E. Macchi and M. Astolfi, *Organic Rankine Cycle (ORC) Power Systems: Technologies and Applications* (Elsevier, 2017).

[4]K. Brun, P. Friedman, and R. Dennis, *Fundamentals and Applications of Supercritical Carbon Dioxide (SCO2) Based Power Cycles* (Elsevier, 2017), pp. xv–xvii.

[5]C. Arpagaus, F. Bless, M. Uhlmann, J. Schiffmann, and S. S. Bertsch, "High temperature heat pumps: Market overview, state of the art, research status, refrigerants, and application potentials," Energy **152**, 985–1010 (2018).

[6]A. Giuffre' and M. Pini, "Design guidelines for axial turbines operating with non-ideal compressible flows," J. Eng. Gas Turbines Power **143**, 011004 (2021).

[7]S. Bahamonde, M. Pini, C. De Servi, A. Rubino, and P. Colonna, "Method for the preliminary fluid dynamic design of high-temperature mini-organic Rankine cycle turbines," J. Eng. Gas Turbines Power **139**, 082606 (2017).

[8]K. Rosset, V. Mounier, E. Guenat, and J. Schiffmann, "Multi-objective optimization of turbo-ORC systems for waste heat recovery on passenger car engines," Energy **159**, 751–765 (2018).

[9]C. M. De Servi, M. Burigana, M. Pini, and P. Colonna, "Design method and performance prediction for radial-inflow turbines of high-temperature mini-organic Rankine cycle power systems," J. Eng. Gas Turbines Power **141**, 091021 (2019).

[10]A. Romei, P. Gaetani, A. Giostri, and G. Persico, "The role of turbomachinery performance in the optimization of supercritical carbon dioxide power systems," J. Turbomach. **142**, 071001 (2020).

[11]N. D. Baltadjiev, C. Lettieri, and Z. S. Spakovszky, "An investigation of real gas effects in supercritical CO_2 centrifugal compressors," J. Turbomach. **137**, 091003 (2015).

[12]J. Schiffmann and D. Favrat, "Design, experimental investigation and multi-objective optimization of a small-scale radial compressor for heat pump applications," Energy **35**, 436–450 (2010).

[13]J. D. Denton, "The 1993 IGTI scholar lecture: Loss mechanisms in turbomachines," J. Turbomach. **115**, 621–656 (1993).

[14]P. A. Thompson, "A fundamental derivative in gasdynamics," Phys. Fluids **14**, 1843–1849 (1971).

[15]P. A. Thompson and K. C. Lambrakis, "Negative shock waves," J. Fluid Mech. **60**, 187–208 (1973).

[16]H. A. Bethe, "On the theory of shock waves for an arbitrary equation of state," in *Classic Papers in Shock Compression Science*, edited by J. N. Johnson and R. Chéret (Springer New York, New York, NY, 1942), pp. 421–495.

[17]P. Colonna, A. Guardone, and N. R. Nannan, "Siloxanes: A new class of candidate Bethe–Zel'dovich–Thompson fluids," Phys. Fluids **19**, 086102 (2007).

[18]*Nonlinear Waves in Real Fluids*, Courses and lectures/International Centre for Mechanical Sciences No. 315, edited by A. Kluwick (Springer, 1991).

[19]M. S. Cramer and A. Kluwick, "On the propagation of waves exhibiting both positive and negative nonlinearity," J. Fluid Mech. **142**, 9–37 (1984).

[20]C. Zamfirescu, A. Guardone, and P. Colonna, "Admissibility region for rarefaction shock waves in dense gases," J. Fluid Mech. **599**, 363–381 (2008).

[21]A. Kluwick, "Non-ideal compressible fluid dynamics: A challenge for theory," J. Phys.: Conf. Ser. **821**, 012001 (2017).

[22]A. A. Borisov, A. A. Borisov, S. S. Kutateladze, and V. E. Nakoryakov, "Rarefaction shock wave near the critical liquid–vapor point," J. Fluid Mech. **126**, 59–73 (1983).

[23]T. Mathijssen, M. Gallo, E. Casati, N. R. Nannan, C. Zamfirescu, A. Guardone, and P. Colonna, "The flexible asymmetric shock tube (FAST): A Ludwieg tube facility for wave propagation measurements in high-temperature vapors of organic fluids," Exp. Fluids **56**, 195 (2015).

[24]T. Mathijssen, "Experimental observation of non-ideal compressible fluid dynamics: With application in organic Rankine cycle power systems," Ph.D. thesis (Delft University of Technology, 2017).

[25]G. Cammi, A. Spinelli, F. Cozzi, and A. Guardone, "Automatic detection of oblique shocks and simple waves in Schlieren images of two-dimensional supersonic steady flows," Measurement **168**, 108260 (2021).

[26]G. Cammi, C. C. Conti, A. Spinelli, and A. Guardone, "Experimental characterization of nozzle flow expansions of siloxane mm for orc turbines applications," Energy **218**, 119249 (2021).

[27]A. Kluwick and E. A. Cox, "Steady small-disturbance transonic dense gas flow past two-dimensional compression/expansion ramps," J. Fluid Mech. **848**, 756–787 (2018).

[28]D. Vimercati, G. Gori, and A. Guardone, "Non-ideal oblique shock waves," J. Fluid Mech. **847**, 266–285 (2018).

[29]D. Vimercati, A. Kluwick, and A. Guardone, "Oblique waves in steady supersonic flows of Bethe–Zel'dovich–Thompson fluids," J. Fluid Mech. **855**, 445–468 (2018).

[30]A. Kluwick and E. A. Cox, "Weak shock reflection in channel flows for dense gases," J. Fluid Mech. **874**, 131–157 (2019).

[31]D. Vimercati, A. Kluwick, and A. Guardone, "Shock interactions in two-dimensional steady flows of Bethe–Zel'dovich–Thompson fluids," J. Fluid Mech. **887**, A12 (2020).

[32]A. Kluwick, "Transonic nozzle flow of dense gases," J. Fluid Mech. **247**, 661–688 (1993).

[33]M. S. Cramer and R. N. Fry, "Nozzle flows of dense gases," Phys. Fluids A **5**, 1246–1259 (1993).

[34]A. Guardone and D. Vimercati, "Exact solutions to non-classical steady nozzle flows of Bethe–Zel'dovich–Thompson fluids," J. Fluid Mech. **800**, 278–306 (2016).

[35]J. D. Anderson, *Modern Compressible Flow: With Historical Perspective*, 2nd ed. (McGraw-Hill, 1990).

[36]G. H. Schnerr and P. Leidner, "Diabatic supersonic flows of dense gases," Phys. Fluids A **3**, 2445–2458 (1991).

[37]M. S. Cramer, J. F. Monaco, and B. M. Fabeny, "Fanno processes in dense gases," Phys. Fluids **6**, 674–683 (1994).

[38]M. S. Cramer, "Rayleigh processes in single-phase fluids," Phys. Fluids **18**, 016101 (2006).

[39]W. C. Reynolds and P. Colonna, *Thermodynamics: Fundamentals and Engineering Applications* (Cambridge University Press, 2018).

[40]D. A. Kouremenos and K. A. Antonopoulos, "Isentropic exponents of real gases and application for the air at temperatures from 150 K to 450 K," Acta Mech. **65**, 81–99 (1987).

[41]N. Baltadjiev, "An investigation of real gas effects in supercritical CO2 compressors," Ph.D. thesis (Massachussets Institute of Technology, 2012).

[42]V. Arp, J. M. Persichetti, and G.-B. Chen, "The Grüneisen parameter in fluids," J. Fluids Eng. **106**, 193–200 (1984).

[43]P. Mausbach, A. Köster, G. Rutkai, M. Thol, and J. Vrabec, "Comparative study of the Grüneisen parameter for 28 pure fluids," J. Chem. Phys. **144**, 244505 (2016).

[44]V. Arp, "Thermodynamics of single-phase one-dimensional fluid flow," Cryogenics **15**, 285–289 (1975).

[45]L. R. F. Henderson, "General laws for propagation of shock waves through matter," in *Handbook of Shock Waves* (Elsevier, 2001), pp. 143–183.

[46]P. Mausbach and H. O. May, "Direct molecular simulation of the Grüneisen parameter and density scaling exponent in fluid systems," Fluid Phase Equilib. **366**, 108–116 (2014).

[47]R. Casalini, U. Mohanty, and C. M. Roland, "Thermodynamic interpretation of the scaling of the dynamics of supercooled liquids," J. Chem. Phys. **125**, 014505 (2006).

[48]A. Guardone and B. M. Argrow, "Nonclassical gasdynamic region of selected fluorocarbons," Phys. Fluids **17**, 116102 (2005).

[49]P. Colonna and A. Guardone, "Molecular interpretation of nonclassical gas dynamics of dense vapors under the van der Waals model," Phys. Fluids **18**, 056101 (2006).

[50]J. Harinck, A. Guardone, and P. Colonna, "The influence of molecular complexity on expanding flows of ideal and dense gases," Phys. Fluids **21**, 086101 (2009).

[51]E. W. Lemmon, I. H. Bell, M. L. Huber, and M. O. McLinden, *NIST Standard Reference Database 23: Reference Fluid Thermodynamic and Transport Properties-REFPROP, Version 10.0* (National Institute of Standards and Technology, 2018).
[52]C. M. Invernizzi, *Closed Power Cycles*, Lecture Notes in Energy, Vol. 11 (Springer London, London, 2013).
[53]A. P. S. Wheeler and J. Ong, "The role of dense gas dynamics on organic Rankine cycle turbine performance," J. Eng. Gas Turbines Power **135**, 102603 (2013).
[54]A. H. Shapiro, *The Dynamics and Thermodynamics of Compressible Fluid Flow* (The Ronald Press Company, 1953), Vol. 1.
[55]E. M. Greitzer, C. S. Tan, and M. B. Graf, *Internal Flow: Concepts and Applications* (Cambridge University Press, 2004).
[56]A. Spinelli, G. Cammi, S. Gallarini, M. Zocca, F. Cozzi, P. Gaetani, V. Dossena, and A. Guardone, "Experimental evidence of non-ideal compressible effects in expanding flow of a high molecular complexity vapor," Exp. Fluids **59**, 126 (2018).
[57]M. Thol, F. H. Dubberke, E. Baumhögger, J. Vrabec, and R. Span, "Speed of sound measurements and fundamental equations of state for octamethyltrisiloxane and decamethyltetrasiloxane," J. Chem. Eng. Data **62**, 2633–2648 (2017).
[58]W. M. Kirkland, "A polytropic approximation of compressible flow in pipes with friction," J. Fluids Eng. **141**, 121404 (2019).
[59]P. Colonna, T. P. van der Stelt, and A. Guardone, "FluidProp (version 3.1): A program for the estimation of thermophysical properties of fluids," a computer program since 2004 (2019), see http://www.asimptote.nl/software/fluidprop.
[60]L. Sciacovelli, P. Cinnella, and X. Gloerfelt, "Direct numerical simulations of supersonic turbulent channel flows of dense gases," J. Fluid Mech. **821**, 153–199 (2017).
[61]R. Dean, "Reynolds number dependence of skin friction and other flow variables in two-dimensional rectangular duct flow," J. Fluids Eng. **100**(2), 215–223 (1978).
[62]M. Pini and C. De Servi, "Entropy generation in laminar boundary layers of non-ideal fluid flows," in *Non-Ideal Compressible Fluid Dynamics for Propulsion and Power*, Lecture Notes in Mechanical Engineering (Springer, 2020), pp. 104–117.
[63]C. F. Colebrook and C. M. White, "Experiments with fluid friction in roughened pipes," Proc. R. Soc. A **161**, 1–15 (1937).
[64]P. Spalart and S. Allmaras, "A one-equation turbulence model for aerodynamic flows," in *Proceedings of 30th Aerospace Sciences Meeting and Exhibit* (American Institute of Aeronautics and Astronautics, Reno, NV, USA, 1992).
[65]G. J. Otero R., A. Patel, R. Diez S., and R. Pecnik, "Turbulence modelling for flows with strong variations in thermo-physical properties," Int. J. Heat Fluid Flow **73**, 114–123 (2018).
[66]L. Sciacovelli, P. Cinnella, and X. Gloerfelt, "*A priori* tests of RANS models for turbulent channel flows of a dense gas," Flow, Turbul. Combust. **101**, 295–315 (2018).
[67]I. Ansys, Ansys CFX release 19.1, 2019.
[68]T. Chen, B. Yang, M. Robertson, and R. Martinez-Botas, "Direct numerical simulation of real-gas effects within turbulent boundary layers for fully developed channel flows," in *Proceedings of Global Power and Propulsion Society GPPS - Chania20* (2020), p. 0068.
[69]C. Crane, "Flow of fluids through valves, fittings and pipe," Technical Report No. 410, NY, 1982.
[70]J. B. Young and R. C. Wilcock, "Modeling the air-cooled gas turbine: Part 1—General thermodynamics," J. Turbomach. **124**, 207–213 (2002).
[71]P. W. Bridgman, "A complete collection of thermodynamic formulas," Phys. Rev. **3**, 273–281 (1914).